South Dakota State University

Open PRAIRIE: Open Public Research Access Institutional Repository and Information Exchange

2023

The Development of Dark Hyperspectral Absolute Calibration Model Using Extended Pseudo Invariant Calibration Sites at a Global Scale: Dark EPICS-Global

Padam Bahadur Karki
South Dakota State University, padam.karki@jacks.sdstate.edu

Recommended Citation

THE DEVELOPMENT OF DARK HYPERSPECTRAL ABSOLUTE CALIBRATION

MODEL USING EXTENDED PSEUDO INVARIANT CALIBRATION SITES AT A

GLOBAL SCALE: DARK EPICS-GLOBAL

BY

PADAM BAHADUR KARKI

A thesis submitted in partial fulfillment of the requirements for the

Master of Science

Major in Electrical Engineering

South Dakota State University

2023

THESIS ACCEPTANCE PAGE

Padam Bahadur Karki

This thesis is approved as a creditable and independent investigation by a candidate for

the master's degree and is acceptable for meeting the thesis requirements for this degree.

Acceptance of this does not imply that the conclusions reached by the candidate are

necessarily the conclusions of the major department.

Morakot Kaewmanee

Advisor   Date

George Hamer

Department Head   Date

Nicole Lounsbery, PhD
Director, Graduate School   Date

I dedicate this work to my grandparents, Fatta Bahadur Karki and Laxmi Karki, my mother, Nir Maya Karki, my daddy, Ram Bahadur Karki, my wife, Manisha Rauniyar, my brother, Sujan Karki, and my sister, Pabitra Karki, Bhagwati Karki, and Pratiksha Karki. None of this may have been possible without their love and support.

"Success isn't always about greatness. It's about consistency. Consistent hard work leads to success. Greatness will come."

Dwayne Johnson

ACKNOWLEDGEMENTS

CONTENTS

ABBREVIATIONS

ALI	Advanced Land Imager
BQA	Pixel quality Assessment Band
BRDF	Bidirectional Reflectance Distribution Function
DAHAC	Dark Hyperspectral Absolute Calibration
DaHD	Dark Hyperspectral Dataset
EO-1	Earth Observing One
EPICS-NA	Extended Pseudo Invariant Calibration Site in North African Desert Sites
ESA	European Space Agency
ExPAC	Extended PICS Absolute Calibration
GC-36	Global Cluster - 36
GDAL	Geospatial Data Abstraction Library
KML	Keyhole Markup Language
L7	Landsat-7
L8	Landsat-8
L9	Landsat-9
MSI	Multispectral Instrument
OLI	Operational Land Imager
PICS	Pseudo Invariant Calibration Sites
S2B	Sentinel-2B
SAA	Solar Azimuth Angle

SZA   Solar Zenith Angle

TIRS   Thermal Infrared Sensor

TOA   Top of the Atmosphere

VAA   View Azimuth Angle

VZA   View Zenith Angle

LIST OF FIGURES

LIST OF TABLES

ABSTRACT

THE DEVELOPMENT OF DARK HYPERSPECTRAL ABSOLUTE CALIBRATION

MODEL USING EXTENDED PSEUDO INVARIANT CALIBRATION SITES AT A

GLOBAL SCALE: DARK EPICS-GLOBAL

PADAM BAHADUR KARKI

2023

This research aimed to develop a novel dark hyperspectral absolute calibration (DAHAC) model using stable dark targets of "Global Cluster - 36" (GC-36), one of the clusters from "300 Class Global Classification." The stable dark sites were identified from GC-36 called "Dark EPICS-Global" covering the surface types viz; dark rock, volcanic area, and dark sand. The Dark EPICS-Global shows a temporal variation of 0.02 unit reflectance. This work uses the Landsat-8 (L8) Operational Land Imager (OLI) , Sentinel-2A (S2A) Multispectral Instrument (MSI) , and Earth Observing One (EO-1) Hyperion data for the DAHAC model development, where well-calibrated L8 and S2A are used as the reference sensors while EO-1 Hyperion with 10 nm spectral resolution is used as a hyperspectral library. The dark hyperspectral dataset (DaHD) is generated by combining the normalized hyperspectral profile of L8 and S2A for the DAHAC model development. The DAHAC model developed in this study takes into account the solar zenith and azimuth angles as well as the view zenith and azimuth angles in Cartesian coordinates form. This model is capable of predicting TOA reflectance in all existing spectral bands of any sensor. The DAHAC model was then validated with Landsat-7 (L7) , Landsat-9 (L9) , and Sentinel-2B (S2B) satellites from their launch dates to March 2022. These satellite sensors vary in terms of

their spectral resolution, equatorial crossing time, spatial resolution, etc. The comparison between the DAHAC model and satellite measurements shows accuracy within 0.01 unit reflectance across overall spectral bands. The proposed DAHAC model uncertainty level is determined using Monte Carlo Simulation and found to be 0.04 and 0.05 unit reflectance for VNIR and SWIR channels, respectively. The DAHAC model double ratio is used as a tool to perform the inter-comparison between two satellites. The sensor inter-comparison results for L8 and L9 shows a 2% difference and 1% for S2A and S2B across all spectral bands.

CHAPTER 1   INTRODUCTION

Satellite imagery is a means to uncover the earth's changes, however, it is critical to

have credible data for scientific study, which is obtained by optical satellite sensors. A wide

range of applications, including atmospheric physics and geoscience, make use of physical

quantities converted from the digital data recorded from satellite images. The reflection or

emission of radiation by the Earth's surface or atmosphere is being used by satellites,

allowing the retrieval of the corresponding physical quantities. Although voltage or

recorded digital data serves as the sensors' primary measuring quantity, calibration must be

carried out to compare the sensor-derived digital data with incoming radiance in their

physical interest. At present, satellite instruments are typically well-designed and calibrated

before launch. Though the satellite equipment is advanced and robust, they eventually

deteriorate in space owing to factors including temperature, mechanical, electrical, or UV

radiation exposure [1]. In order to ensure the quality of the derived variables and products,

reliable remote sensing relies on a sensor re-calibration commonly called radiometric

calibration [2].

1.1   Absolute Radiometric Calibration

Data evaluation and quality of satellite data highly depend on the absolute

radiometric calibration of the sensor. During the absolute calibration process, the satellite

images are processed and converted into digital numbers, or the measured voltage in the

form of physical quantities such as at-sensor spectral radiance or top of the atmosphere

(TOA) reflectance [3], [4]. The absolute calibration approach helps in characterizing and

measuring the sensor's performance from the early pre-launch stage to its on-orbit

operation. Calibration can also be performed using different methods, for example, pre-launch, onboard, and vicarious calibration. The results of post-launch calibration are compared with pre-launch calibration using several different methods in lab [5]. After the satellite is placed in its orbit, the sensor characterization and its accuracy measurement are needed throughout its lifetime. Onboard calibrators, such as solar diffuser panels, lamps, etc., can be used to perform radiometric calibration [6], [7]. However, onboard calibrators require routine operation and maintenance. They are expensive and also prone to the effects of harsh conditions in the space environment. For these reasons, many satellite sensors do not include onboard calibration. In order to overcome these limitations, Pseudo Invariant Calibration Sites (PICS) were discovered for satellite calibration. The satellite imagery over the PICS across the earth's surface is spatially, temporally, and spectrally stable [8].

1.2 Stable Calibration Sites

Several studies on PICS-based assessment have been performed to identify the stable pixels for sensor radiometric stability for more than 20 years[3]. Spatially uniform PICS sites exhibit stable spectral features over time, higher reflectance, and no atmospheric influence on upward radiation [9]. A spatial uniformity of at least 3% and temporal variability of 1% – 2% was found by Cosnefroy et al. over twenty desert locations [10]. Six PICS for North Africa that the Committee on Earth Observation Satellites (CEOS) recommended showing temporal variability in all bands of 3% or less [11]. According to Helder et al., Libya 4, Libya 1, Algeria 3, Arabia 2, Egypt 2, and Egypt 1 had variability of less than 3% and were capable of monitoring long-term trends [8]. Research studies on identifying stable pixels were then conducted by South Dakota State University Image

Processing Laboratory (SDSU IP Lab) to identify the best locations with 3% or less of temporal, spatial, and spectral variability. Less temporal uncertainty was considered in Libya 4, Niger 1, Sudan 1, Niger 2, Egypt 1, and Libya 1. With a temporal variation of less than 3%, Libya 4 stood out as the most consistently stable site among them and could be widely employed in radiometric calibration work[3], [12]–[14]. Shrestha et al. [6] applied the K-means unsupervised classification method, which resulted in identifying 19 clusters representing distinct land surface types in North Africa with pixels having 5% or less of both the spatial and temporal uncertainty. Fajardo et al. expanded the unsupervised classification to 160 clusters at a global scale and identified a cluster with stable bright sites named "global EPICS" [5]. The global EPICS showed a temporal variation of less than 4% for all bands, with some as low as 2.7%. The global classification with 160 clusters was further improved by the author to develop the "300 Class Global Classification" with its 300 clusters around the globe [15]. Past studies, including the research at SDSU IP Lab, focused on absolute calibration using stable bright sites i.e., PICS. However, the absolute calibration model developed in the past works neither covers the dynamic range of reflectance measurements nor developed the calibration model using stable dark targets at a global scale. This work proposed an algorithm to build an absolute calibration model using low reflectance dark targets capable of performing satellite calibration in addition to a bright target absolute calibration model. In this study, low reflectance measurements are identified from the stable dark targets of "Global Cluster - 36" (GC-36) , one of the clusters from "300 Class Global Classification." This study uses the identified stable dark targets of the GC-36, named "Dark EPICS-Global."

1.3   Evolution on Development of Absolute Calibration Model

Govaerts et al. [16] developed an absolute calibration model using the PICS for geostationary satellite sensors. To characterize the atmospheric effects more accurately, an advanced radiative transfer model was developed for Libya 4 sites in 2012. The expanded model included the polarization effects and non-spherical aerosol models and showed accuracy within 3% [17]. In 2010, Helder et al. developed the concept of an empirical absolute calibration model using PICS and the Terra Moderate Resolution Imaging Spectroradiometer (MODIS) as a reference sensor. The model was validated with Landsat-7 (L7) with an accuracy of 3% and 6% for the visible and short wave infrared (SWIR) channels, respectively [12]. Based on daily radiance observations over Libya 4 using a geostationary Earth orbit (GEO) sensor, Bhatt et al. developed a desert daily exoatmospheric radiance model (DERM) [18]. The model accuracy remained consistent within 0.4% and 1.9% for Meteosat-8 and Meteosat-7 with the reference Meteosat-9 DERM. Likewise, GOES-11 DERM showed an accuracy of 1% and 3% while calibrating GOES-10 and GOES-15, respectively [19]. In order to minimize the Bidirectional Reflectance Distribution Function (BRDF) impact generated by the sensor's off-nadir observations and seasonal fluctuations owing to solar position shift, Mishra et al. [4] considered a View Zenith Angle (VZA) for the absolute calibration model. Using Terra MODIS as a reference sensor, this model achieved 3% accuracy and uncertainty within 2% for six spectral bands [4]. In 2017, the Coastal Aerosol band was included as part of an improvement to the existing absolute calibration model using data from Landsat-8 (L8) images named as refined absolute calibration model. The accuracy of the refined absolute calibration model was

within 3% for all spectral bands [20]. Raut et al. [3] expanded the absolute calibration

model considering five additional Saharan Desert PICS and found the model performance

within 3% accuracy with 2% precision for three sites viz; Egypt 1, Libya 1, and Sudan 1.

However, due to a lack of insufficient reliable Hyperion data, the model performance

showed less accuracy for Niger 1, and Niger 2 [3].

In the previous studies, the scene center-specific spherical angle was used to develop

a BRDF model to finalize the absolute calibration model [3], [4], [12]. The reprocessing of

the Landsat archive was performed in 2017, including the geometric error of 12 m Root

Mean Square Error and 3% radiometric uncertainty [21]. All Landsat Collection-1 data

produced by this method contains files including the sun illumination and sensor viewing

angle coefficients as well as details about the quality assessment (QA) bands. Using the

existing information in the Level-1 product of Landsat-8, Farhad et al. developed a novel 4

angle BRDF model using the solar and view geometry angles in the form of Cartesian

coordinates. This 4 angle BRDF model preserves the data nature to achieve a robust fit. The

estimated temporal variation across all the spectral bands was within 1.8% over Libya 4

PICS [22]. In 2019, the Extended PICS Absolute Calibration (ExPAC) model with solar and

view angles was developed using Extended Pseudo Invariant Calibration Site in North

African Desert Sites (EPICS-NA) as a target and L8 as a reference sensor. The ExPAC

model showed a prediction accuracy of 2% after validation with L7, L8, Sentinel-2A (S2A),

and Sentinel-2B (S2B) sensors[23]. Chaity et al. developed an empirical hyperspectral

absolute calibration model for Libya 4 PICS (hyperspectral APICS) using L8 Operational

Land Imager (OLI) and Earth Observing One (EO-1) Hyperion sensors [1]. To better

represent the angles, the hyperspectral APICS model used pixel-wise 4 angle BRDF

information in Cartesian coordinates. This model had the potential to perform absolute calibration in 1 nm spectral resolution and showed the accuracy and precision of 6% and 4%, respectively for the off-nadir viewing sensor. Similarly, the model showed accuracy and precision of 3% for the nadir viewing sensor, respectively [1]. However, the hyperspectral APICS model was constrained for the Libya-4 PICS site and showed poor performance for non-Landsat bands, although this could be improved.

1.4   Objectives of the Study

The main objective of this study is to develop a novel Dark Hyperspectral Absolute Calibration (DAHAC) model using L8, S2A, and EO-1 Hyperion measurements over the identified stable dark sites (Dark EPICS-Global) of "Global Cluster - 36" (GC-36). L8 OLI and S2A MSI are used as reference sensors, and EO-1 Hyperion as the hyperspectral library to convert the multispectral profile of L8 and S2A in the hyperspectral domain. The dark hyperspectral data and their angular information in the Cartesian coordinate form are used to build the 4 angle hyperspectral BRDF model which is further simplified to develop the DAHAC model. Unlike Chaity's development, the proposed model is unique with its novel algorithm to develop a more accurate model using the "low reflectance measurements" at a global scale. The DAHAC model is capable of predicting the Top of Atmosphere (TOA) reflectance in all existing hyperspectral bands for any sensors. The DAHAC model validation is performed with respect to L7, S2B, and Landsat-9 OLI (L9). Furthermore, the DAHAC model double ratio is estimated to perform sensor inter-comparison between L8 and L9 for Landsats and S2A and S2B for Sentinel-2(s).

1.5   Thesis Outline

This thesis is organized into the following sections: Chapter1 illustrates the background and literature review on radiometric calibration along with the absolute calibration model development techniques based on PICS and its evolution towards EPICS Global. Chapter 2 outlines sensor characteristics used in this study, the selection of dark targets for the study area and its validation, Dark Hyperspectral Dataset generation, and the DAHAC model development process. Chapter 3 discusses the DAHAC model validation results with respect to several sensors. Chapter 4 presents the DAHAC model uncertainty estimation process. Chapter 5 describes the sensor inter-comparison based on the DAHAC model double ratio estimation. Finally, Chapter 6 summarizes and concludes the thesis.

CHAPTER 2   METHODOLOGY

This section explains the development of the Dark Hyperspectral Absolute Calibration (DAHAC) model using reflectance measurements of L8, S2A, and EO-1 over Dark EPICS-Global. Fig. 2.1 shows the overall architecture of study area selection and sensor data pre-processing for generating the dark hyperspectral dataset required for the DAHAC model development. This work started with a thorough analysis of different satellite sensors viz; L7, L8, L9, S2A, S2B, and EO-1 Hyperion. The multispectral sensors (L8 and S2A) are utilized as reference sensors, and EO-1 is used as a hyperspectral library source. The preliminary selection and identification of many dark targets around the globe from 300 global clusters is the first major step. GC-36 is selected as the most suitable dark target as its spectral response is closely similar to the volcanic site used for the cross-calibration of S2A, and L8 [22]. In this study, the selected dark sites from GC-36 are validated by comparing their TOA reflectance with the overall GC-36 TOA reflectance measurements to provide a Dark EPICS-Global. Furthermore, this section also explains the detailed process to generate the normalized hyperspectral profile for two multispectral sensors, L8 and S2A, using the EO-1 Hyperion as a hyperspectral library. The procedures to generate the Dark Hyperspectral Dataset for creating the 4 angle BRDF model are also presented in detail. Finally, the process of developing the DAHAC model from the 4 angle BRDF model is also discussed in the sections below.
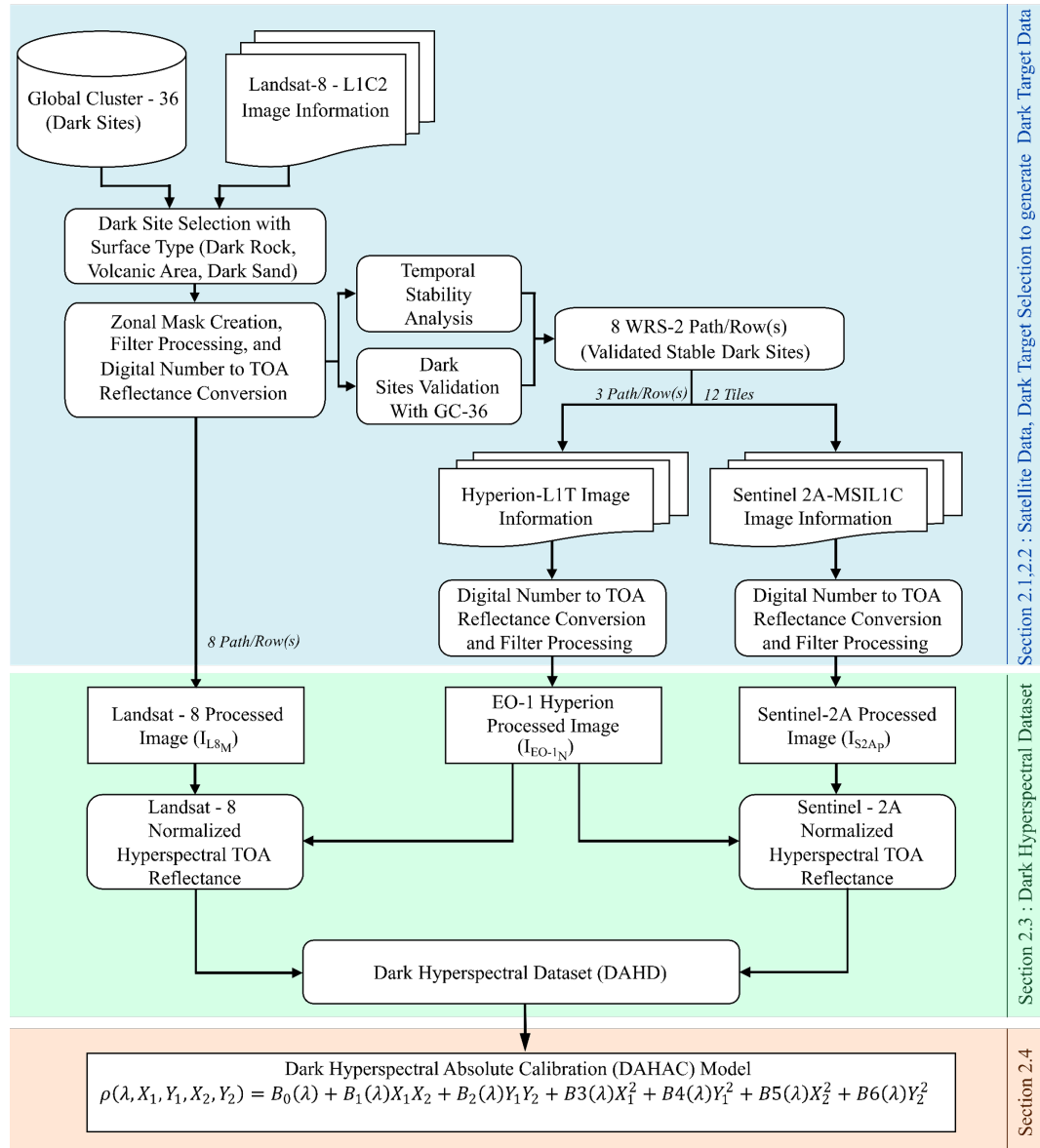
Figure 2.1. Flowchart showing study area selection and sensor pre-processing for the DAHAC model development.

2.1 Satellite Data

2.1.1 Landsat-7,8,9

Since 1972, Landsat missions have continuously collected multispectral data covering the entire planet with a temporal resolution of 16 days. L7, which was launched on April 15, 1999, has eight spectral bands and operates at a mean altitude of 705 km in a

sun-synchronous orbit. Prior to the launch of L8, L7 had a satellite calibration of 5%,

making it the most stable sensor within the Landsat family. [7]. However, Scan Line

Corrector (SLC) issues with L7 have existed since May 2003 and have resulted in scenes

with wedge-shaped data gaps [24]. The radiometric stability of the ETM+ satellite has been

evaluated with the help of on-orbit calibration and vicarious measurements. The partial and

full-aperture solar calibration is continuously performed by taking the source as the sun for

onboard calibrators [25]. The official science mission of L7 ended on April 6, 2022. L7

started its extended science mission on May 5, 2022, from a lower orbit of 697 kilometers

[26].

L8 is part of the Landsat series, which was launched on February 11, 2013. It has

two different instruments: an OLI sensor and Thermal Infrared Sensor (TIRS) . L8 has been

producing high-quality image information for earth observation with spatial resolutions of

30m for eight separate spectral bands and 15m for the panchromatic band. The uncertainty

associated with the L8 post-launch reflectance calibration is within 2% [7]. The

improvement in the Landsat image product was performed in 2018, which provided a

level-1 product with angle information and the quality assessment band. The radiometric

calibration was updated in Coastal Aerosol, and Blue band for the level-1 collection-2

product [27].

The most recent satellite in the Landsat constellation is Landsat 9, which was

launched on September 27, 2021. Landsat 9 is an identical instrument to Landsat 8 with

better radiometric resolution. Increased quantization from 12 to 14 bits in L9 enables the

sensor to acquire more small variations resulting to give better image quality. The

sun-synchronous orbit of L9 is at an altitude of 705 km and takes 16 days to complete one

orbit cycle [28].

Eq. 2.1 showing the conversion of Landsat imagery digital number (DN) values to TOA reflectance [29].

$$\rho_{observed} = \frac{M_\rho \times Q_{Cal} + A_\rho}{cos\alpha} \tag{2.1}$$

Where M_ρ and A_ρ are the multiplicative and additive factors in metadata format, Q_{Cal} represents the calibrated DN value and α is the solar zenith angle.

2.1.2   Sentinel-2A,2B

The European Space Agency (ESA) launched S2A on 23 June 2015 and S2B on 7 March 2017 under the Copernicus program. S2A and S2B are positioned in a sun-synchronous orbit at an altitude of 786 km, phased at 180° relative to one another. These sensors are equipped with push-broom sensor multi-spectral instruments (MSI) that measure the solar reflectance for 13 different spectral bands with 10m, 20m, and 60m spatial resolution. The orbital period and combined orbital period for these two satellites are ten days, and five days, respectively. The MSI focal plane detectors are divided into 12 different modules to allow these sensors to provide an image with a 290 km swath width at a 20.6° field of view [30], [31]. In 2017, the study on sentinel-2 satellite showed that the absolute calibration was better than 5% for overall sensor spectral bands [32]. European Space Agency reported that Sentinel-2 products would soon be upgraded. Sentinel-2A and 2B have undergone multiple processing systems during the course of their lifetimes. The processed data with a baseline of 2.0 or above, from the launch time to October 2022, are used in this study. The TOA reflectance is calculated using Eq. 2.2 and 2.3.

$$\rho_\lambda = \frac{DN_{cal}}{Q} \tag{2.2}$$

where DN_{cal} represents the calibrated DN value and Q is a scale factor that is equal to

10000. This scaling factor accounted for the Earth-Sun distance, exoatmospheric irradiation,

and cosine correction. The sentinel-2 processing system version 4.0 has been installed since

January 25, 2022. Thus the TOA reflectance conversion equation is updated as shown in Eq.

2.3.

$$\rho_\lambda = \frac{DN_{cal} + Offset}{Q} \tag{2.3}$$

where offset = -1000 is reported in the metadata image information. The estimated TOA

reflectance for S2A is illustrated in Fig. 2.6.

2.1.3   Earth Observing One (EO-1) Hyperion

The EO-1 Hyperion was a hyperspectral satellite that was part of NASA's New

Millennium Program. This satellite was launched on November 21, 2000, and was

discontinued on March 20, 2017 [33]. There were two instruments on board; Advanced

Land Imager (ALI) , a hyperspectral imaging spectrometer, and the Linear Etalon Imaging

Spectral Array (LEISA) Atmospheric Corrector (LAC). The push-broom hyperspectral

sensor covers 400 nm – 2500 nm spectral range and 242 band images (including 196

onboard calibrated bands [34]) with a 10 nm spectral resolution and a 30 m spatial

resolution over a 7.7 km swath width. The EO-1 stability analysis for 16 years of operation

with varying orbital precession reveals calibration uncertainty for all spectral bands within

5% – 10% [35]. The following Eq. 2.4 is used to convert the EO-1 Hyperion DN values to TOA reflectance.

$$\rho_\lambda = \frac{\frac{DN_{cal}}{h} \times \pi \times d^2}{E_{sun} \times sin\phi \times cos\theta} \qquad (2.4)$$

Where DN_{cal} represents the calibrated digital number value, h defines the scale factor, d indicates Earth-Sun distance in A.U. unit, E_{sun} demonstrates the conversion of calibrated radiance to reflectance derived from ChKur solar spectrum (ESUN(ChKur)) [36],ϕ and θ are sun elevation and sensor look angle, respectively. The summarized information for the sensors used in this study is shown in Table. 2.1.

Table 2.1. Showing different sensor information used in the DAHAC model development.

Information	Sensors					
	Landsat-7	Landsat-8	Landsat-9	Sentinel-2A	Sentinel-2B	EO-1 Hyperion
No. of Images	764	1150	84	775	456	64
Image Dates	2000 – 2022	2013 – 2022	2021 – 2022	2015 – 2022	2017 – 2022	2001 – 2017
SZA Range (°)	20 – 58	20 – 60	20 – 60	15 – 51	15 – 54	23 – 77
SAA Range (°)	36 – 160	35 – 160	35 – 158	31 – 164	31 – 165	70 – 145
VZA Range (°)	0.10 – 8	0.03 – 5	0.17 – 8	0.04 – 10	0.09 – 10	0.04 – 25
VAA Range (°)	-94 – 136	-178 – 180	-80 – 118	-89 – 130	-162 – 135	-82 – 98
No. of Sites	8 WRS-2 path/row(s)	8 WRS-2 path/row(s)	8 WRS-2 path/row(s)	12 Tiles	12 Tiles	3 path/row(s)

2.2   Dark Target Selection

This section explains the steps for identifying dark targets by choosing the stable pixels from the dark target clusters under "300 Class Global Classification" using the L8 imagery information. This section also describes the zonal mask creation process and filtering technique.

2.2.1   Identifying Stable Dark Target Using Landsat-8

Three different global clusters, Global Cluster-6 (GC-6), Global Cluster-26 (GC-26), and Global Cluster-36 (GC-36), are discovered to be the dark clusters among the 300 Clusters from the "300 Class Global Classification." These clusters include surface types viz; dark rock, dark sand, volcanic area, dark pond, etc. GC-36 is selected as the dark cluster for this study based on the higher pixel counts and pixel density. Since GC-36 is a GeoTIFF format, Geospatial Data Abstraction Library (GDAL) is used to generate Keyhole Markup Language (KML) files for GC-36. Using a KML file, L8 WRS-2 system, Google Earth Pro, and Earth Explorer program, an initial visual inspection is performed to choose the WRS-2 path/row(s) with surface type: dark rock, dark sand, volcanic area, and vegetation area on each continent. Initially, 13 distinct WRS-2 path/row(s) from the Middle East, South Africa, and North Africa were chosen. However, the surface types viz; dark rock, dark sand, and volcanic area show a similar spectral response as the Libyan volcanic site that was used for cross-calibration purposes between L8 and S2A sensors [22].

Based on the spectral characteristics, eight different WRS-2 path/row(s) are chosen as dark sites for this study. The eight selected WRS-2 path/row(s) have pixel counts within the range of 21726 – 2359755. The 8 WRS-2 path/row(s) in the three continents with

surface type description is illustrated in Table 2.2. The selected WRS-2 path/row(s) for L8,

along with the global map shown in Fig. 2.2. They are further used to perform temporal

stability analysis in Section 2.2.4.

Table 2.2. Showing WRS-2 path/row(s), surface types, and pixel count across different continents.

Continents	Path/Rows	Surface Description	Pixel Count
Middle East	159/40	dark rock	73544
	163/37	dark rock	36070
	168/51	dark rock, dark sand	2359755
	170/42	volcanic area	710696
South Africa	180/75	volcanic area, dark rock	40626
	181/73	dark rock, dark sand	21726
North Africa	183/46	volcanic area	30009
	184/43	volcanic area	133950

a. Middle East

b. North Africa
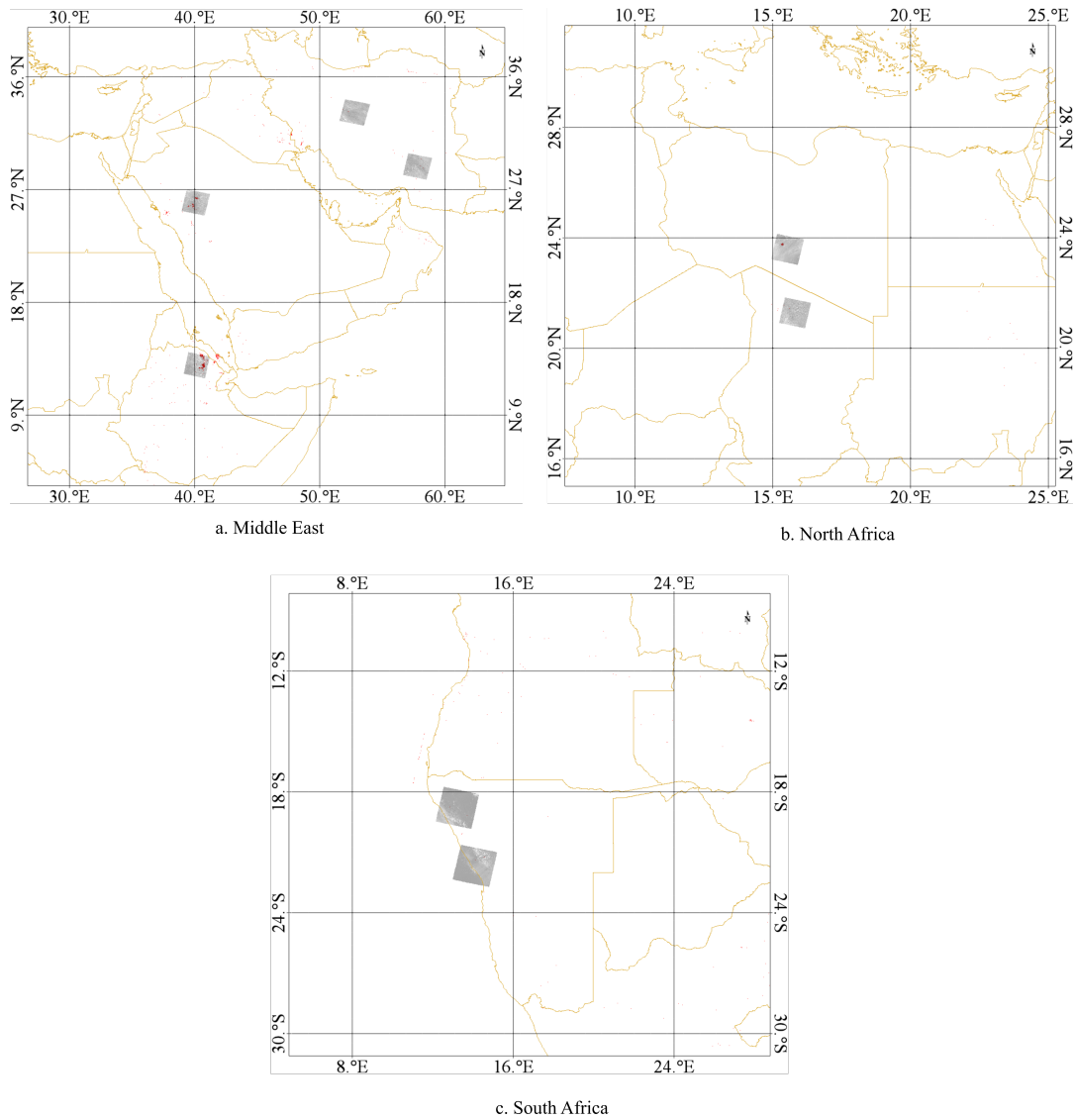
c. South Africa

Figure 2.2. GC-36 stable dark target pixels in red color. WRS-2 Path/Row(s)images footprint for L8 in the different continents: (a) Middle East, (b) South Africa, and (c) North Africa.

2.2.2 Creation of Zonal Mask for Satellites

Following the selected dark pixels location information in Section 2.2.1, a zonal dark pixel mask is generated using *'gdalwarp'* function from the GDAL library based on the spatial resolution of; 10 m, 20 m, 30 m, 60 m, and Universal Transverse Mercator (UTM) zone. To accommodate for images positioned in two distinct UTM zones, the zonal mask is extended by 100 km in the East-West direction.

2.2.3   Filtering and Dark Pixel Validation

The primary goal of applying filters is to obtain a clear pixel by removing the cloud from images. The Landsat products with Level 1 Collection 2 (L1C2) are provided with a Pixel quality Assessment Band (BQA) [37]. Based on the BQA information, a binary cloud mask is built, including fill values, dilated cloud, cirrus, cloud, cloud shadow, cloud confidence, and cloud shadow confidence, which is then applied for each L7, L8, and L9 satellite image. In the case of the Sentinel-2 sensor, the provided binary cloud mask is applied for each Sentinel-2 image. Similarly, to remove the cloudy pixels from Hyperion images, Band-123 (1376 nm) image information with almost 100% absorption feature is used as a binary cloud mask.

Although these cloud binary masks can be employed at the pixel level, we choose to use them first at the scene level to eliminate dates where the region of interest (GC-36 pixels) is substantially obscured by clouds. This is because cloud filters are not perfect and can miss cloudy pixels on days that are extremely cloudy. To remove the cloudy image, a potential threshold containing a clear pixel for each image is determined at 40%. In other words, if the number of clear pixels in the cloud binary mask is larger than 40% of the number of pixels in the satellite images, the image is selected for applying the pixel-by-pixel cloud mask; otherwise, the entire scene is discarded.

Even after filtering the cloud in the sensor images, there could be a chance that the cloud shadow pixel has the same pixel values as of clear dark pixel. The clear dark pixels in the sensor images are validated using reference L8 image information. First, the BQA filter with cloud shadow and cloud shadow confidence is employed on L8 images. L8 images are

also applied to the BQA filter without cloud shadow and cloud shadow confidence. Further, the convolution theory is applied to the resulting two sets of images in order to distinguish the real dark pixels in the images. This process clarified that the pixels associated with each image are clear dark pixels.

2.2.4 Dark Target Data for Absolute Calibration

The cloud-free images are used to estimate the TOA reflectance for each sensor. The estimated TOA reflectance for L8 (1150 images) for dark sites ranges from 0.043 to 0.17, as shown in Fig. 2.3. It can be observed that the selected dark sites are temporally stable with a standard deviation of 0.02 across all the spectral bands. The selected sites (Path/row(s)) for L8 are validated with respect to GC-36 by comparing the estimated TOA reflectance. GC-36 itself is defined in a way that the pixels included within this class represent identical attributes based on unsupervised K-means clustering. The mean and standard deviation of TOA reflectance for each of the selected sites for each band is compared against the mean and 3σ standard deviation of GC-36 as shown in Fig. 2.4. The minimum and maximum 3σ values for GC-36 are shown by red color dotted lines. In Fig. 2.4, it can be observed that for all spectral bands, the estimated mean TOA reflectance for each site is within the boundary line, except for the SWIR-2 band crossing the boundary line within an acceptable range. Therefore, the selected dark sites under GC-36 for the L8 sensor are validated and represented as "Dark EPICS-Global" for this study.

After identifying the Dark EPICS-Global using the L8 as a reference sensor, the location of these selected dark sites is further used to investigate the availability of data for the S2A and EO-1 sensors. Three distinct WRS-path/row(s), i.e., 168/50, 183/46, and
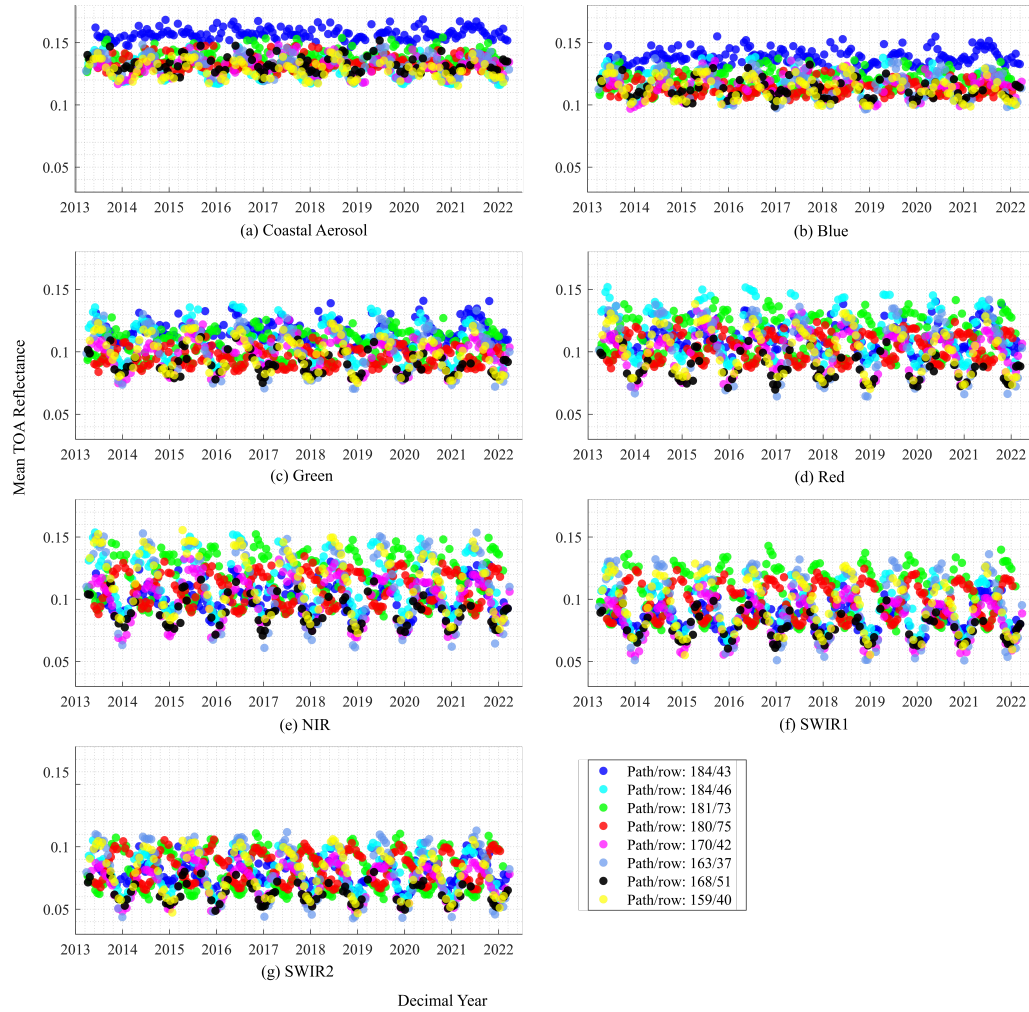
Figure 2.3. L8 dark target TOA reflectance of eight WRS-2 path/row(s) for seven spectral bands.

184/43, are available for the EO-1 sensor. A total of 64 Hyperion images are obtained from the selected stable sites, and their estimated hyperspectral TOA reflectance for the 196 calibrated bands are shown in Fig. 2.5. There are 12 tiles representing the dark sites selected for the S2A sensor, as shown in Fig. 2.6. Fig. 2.6 shows the estimated TOA reflectance using 775 images obtained from the 12 stable dark tiles for the S2A sensor. The TOA reflectance for each tile is within the range of 0.04–0.18, and the standard deviation of 0.02 for all spectral bands. These TOA reflectance estimations using Dark EPICS-Global for L8,
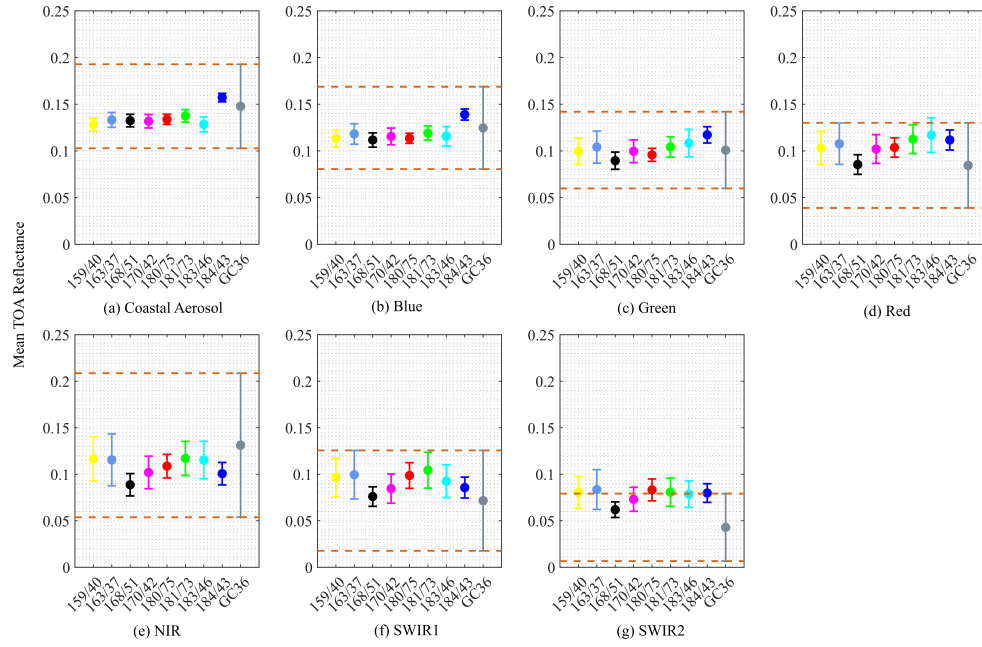
Figure 2.4. TOA reflectance comparison between selected dark target (L8) and GC-36, and red dotted lines showing the 3σ TOA reflectance of GC-36.
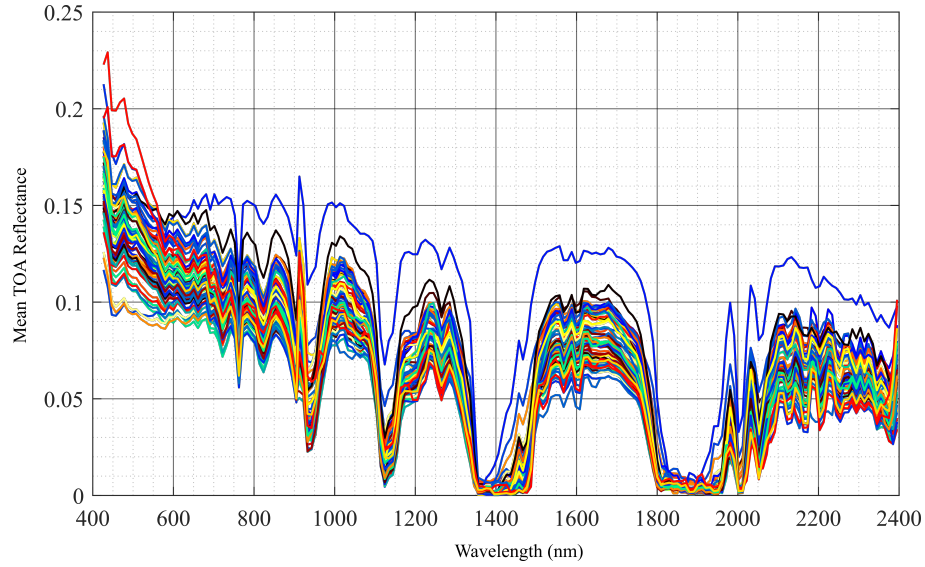
Figure 2.5. EO-1 Hyperion hyperspectral TOA reflectance for 64 images obtained from the selected stable dark sites.

S2A, and EO-1 are named dark target data. The estimated dark target data are further used to generate the Dark Hyperspectral Dataset (DaHD).
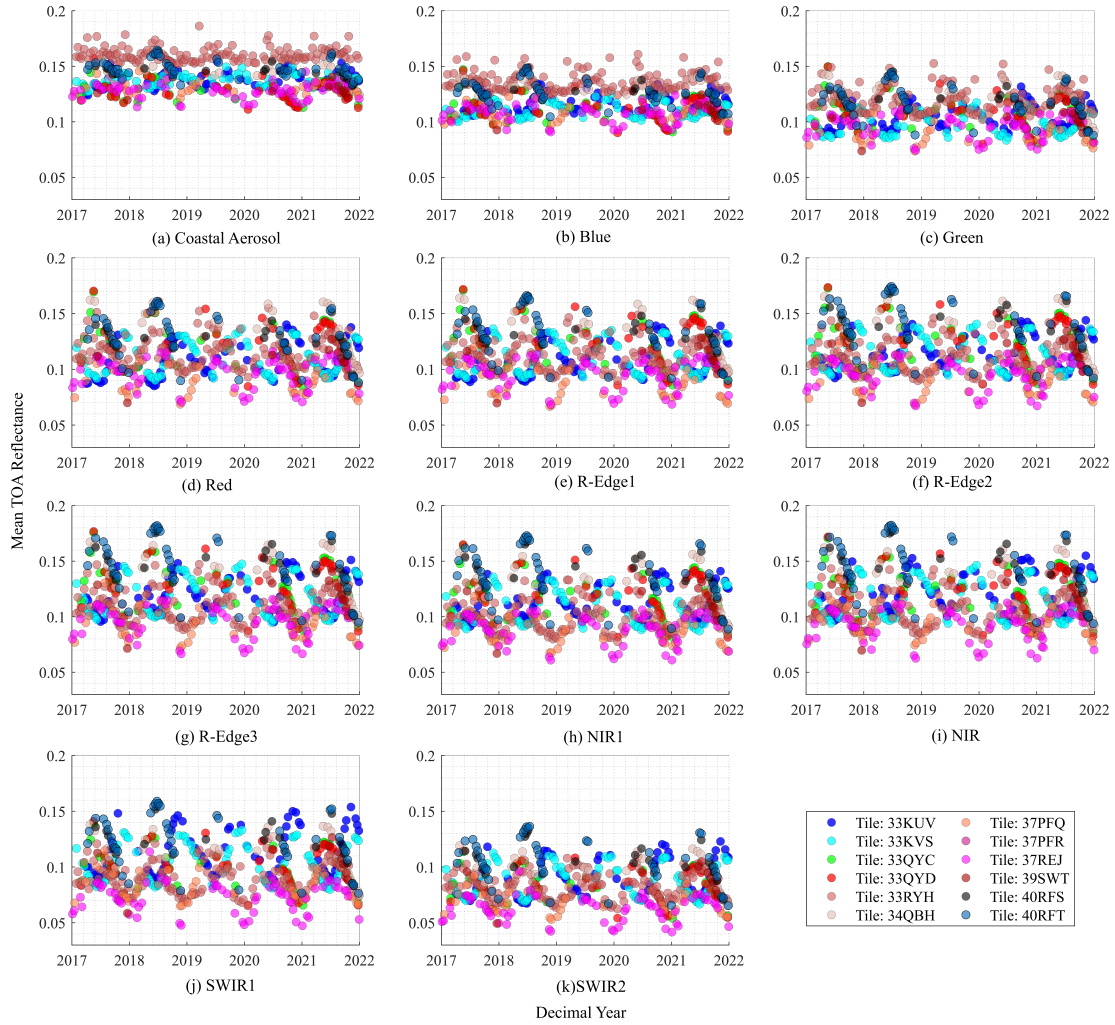
Figure 2.6. TOA reflectance of twelve tiles for S2A spectral bands ranging from 0.04 to 0.18 TOA reflectance.

2.3 Dark Hyperspectral Dataset (DaHD)

This section explains the dark hyperspectral data generation process to develop the hyperspectral absolute calibration model. L8 and S2A are used as reference sensors since they are well-calibrated, and their combination covers a wide range of angular information as well as non-Landsat spectral bands. L8 and S2A have their TOA reflectance measurements in the multispectral domain, which are converted into the hyperspectral domain. The multispectral to hyperspectral profile conversion is done using EO-1 Hyperion

as a hyperspectral library. The hyperspectral profile of L8 and S2A is achieved in two steps

requiring two inputs, "Input 1" and "Input 2," as shown in Fig. 2.7.
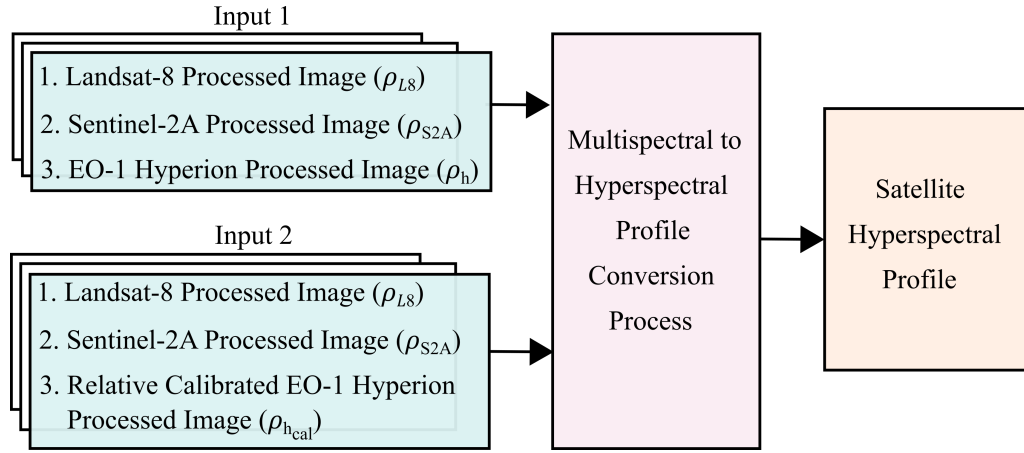
Figure 2.7. Block diagram showing satellite hyperspectral profile generation process.

Input 1 consists of processed image (ρ_{L8}), S2A (ρ_{S2A}), and EO-1 Hyperion (ρ_h).

After going through the process of converting the multispectral domain to the hyperspectral

domain as described in Fig. 2.8, the output is L8 and S2A hyperspectral profile. This

hyperspectral profile is validated with L8 and S2A data to see if they represent the measured

TOA reflectance. It is found that there is some discrepancy between the hyperspectral

profile and the satellite measurements of approximately 1 unit TOA reflectance in CA,

Green, and SWIR2 bands, as shown in Fig. 2.9. Therefore, the EO-1 hyperspectral profile

(ρ_{hcal}) is modified by applying relative gain to Hyperion data as described in Section. 2.3.2.

"Input 2" consisting of ρ_{L8}, ρ_{S2A}, and ρ_{hcal} are used to obtain the final hyperspectral profile

for L8 and S2A. The detailed procedures to convert the multispectral to hyperspectral

profile are explained in the sections below.

2.3.1 Estimation of Satellite Hyperspectral Profile

Figure. 2.8 shows the detailed conversion process of the multispectral profile into its hyperspectral profile.
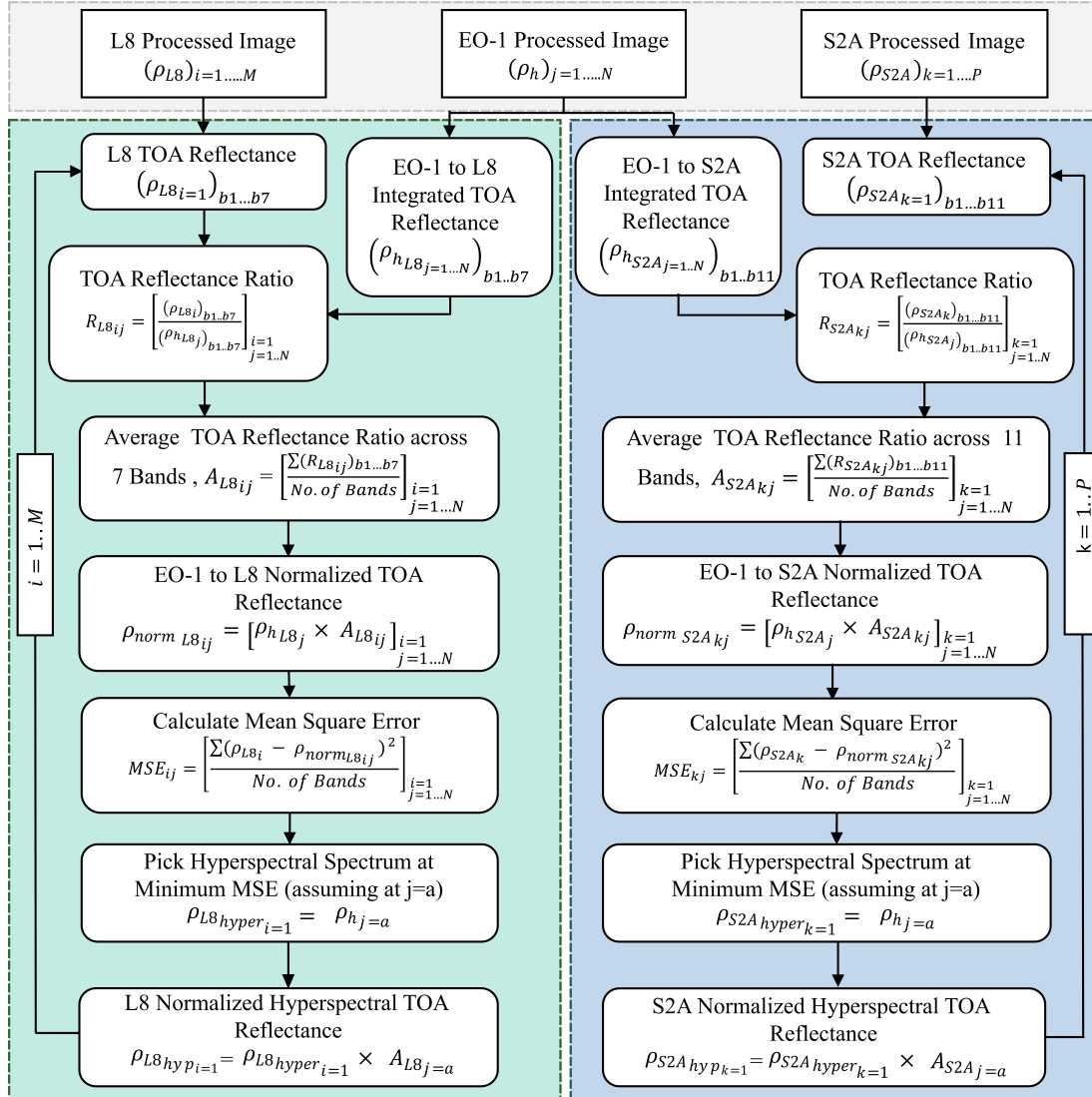
Figure 2.8. Overall flowchart showing the Dark Hyperspectral Dataset generation process.

There are three satellite data; L8 (M = 1150 images), S2A (P = 775 images), and EO-1 (N = 64 images); represented by $(\rho_{L8_{i=1..M}})$, S2A $(\rho_{S2A_{k=1..P}})$, and $(\rho_{h_{j=1..N}})$ respectively. Using Eq. 2.5, the band-integrated TOA reflectance $(\rho_{h_{sat}})$ for satellites viz; L8

$(\rho_{h_{L8_{j=1..N}}})$ and S2A $(\rho_{h_{S2A_{j=1..N}}})$ are estimated by integrating the relative spectral response (RSR) of the reference sensors (RSR_{sat}) with the Hyperion profile (ρ_h) at each sampled wavelength $(d\lambda)$, weighted by the corresponding RSR of reference sensor.

$$\rho_{h_{sat}}(\lambda) = \frac{\int_{\lambda_1}^{\lambda_2} \rho_h \times RSR_{sat} d\lambda}{\int_{\lambda_1}^{\lambda_2} RSR_{sat} d\lambda} \tag{2.5}$$

The TOA reflectance ratio $(R_{L8_{i=1,j}})$ are estimated between L8 TOA reflectance $(\rho_{L8_{i=1}})$ for the first image with respect to N number of EO-1 to L8 integrated TOA reflectance $(\rho_{h_{L8_{j=1..N}}})$ across all the bands (b1...b7). The average TOA reflectance ratio $(A_{L8_{i=1,j=1..N}})$ is taken across the bands for N number of $R_{L8_{i=1,j=1..N}}$. EO-1 to L8 normalized TOA reflectance $\rho_{norm_{L8_{i=1,j=1..N}}}$ are then computed by multiplying $\rho_{h_{L8_{j=1..N}}}$ with $A_{L8_{i=1,j=1..N}}$.Further, mean square error $(MSE_{i=1,j=1..N})$ are calculated among $\rho_{norm_{L8_{j=1...N}}}$ with respect to $\rho_{L8_{i=1}}$ using Eq. 2.6 given below:

$$MSE_{ij} = \frac{\sum(\rho_{sat_i} - \rho_{norm_{sat_{ij}}})^2}{\text{No. of Bands}} \tag{2.6}$$

Where ρ_{sat} and $\rho_{norm_{sat}}$ are the TOA reflectance and normalized TOA reflectance of satellites ("sat" refers to either L8 or S2A). For $\rho_{L8_{i=1}}$,the minimum MSE value is observed from N number of MSEs at instant $j = a$ (say). The final hyperspectral spectrum $(\rho_{L8_{hyper_{i=1}}})$ is then picked from the Hyperion library$(\rho_{h_{j=1..N}})$ at $j = a$. Finally, L8 normalized hypersepctral TOA reflectance $(\rho_{L8_{hyp_{i=1}}})$ is obtained by further multiplying the $\rho_{L8_{hyper_{i=1}}}$ with the average TOA reflectance ratio $(A_{L8_{i=1,j=a}})$ for the first $\rho_{L8_{i=1}}$. This process repeats for $M = 1150$ number of L8 processed images to achieve M number of L8 normalized hyperspectral TOA reflectance profiles. The same process is applied to Sentinel-2A data to

obtain $P = 775$ number of S2A normalized hyperspectral profiles ($\rho_{S2A_{hypP_{k=1..P}}}$).
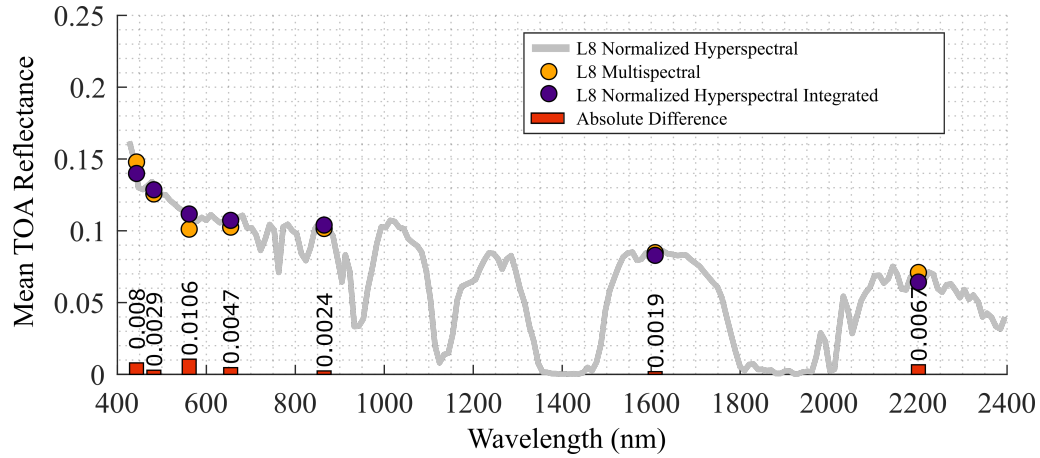
Figure 2.9. Showing L8 normalized hyperspectral TOA reflectance (grey curve), L8 multispectral TOA reflectance (orange circle), L8 normalized hyperspectral integrated TOA reflectance (purple circle), and absolute difference (red bar): before relative calibration.

The normalized hyperspectral TOA reflectance for both L8 ($\rho_{L8_{hypP_i}}$) and S2A ($\rho_{S2A_{hypP_k}}$) are further integrated into its multispectral bands ($\rho_{L8_{hypP_{mult}}}$) and compared with their observed TOA reflectance ($\rho_{L8_{i=1}}$) measurements to check the accuracy of their hyperspectral profile. Fig. 2.9 shows the $\rho_{L8_{i=1}}$ (orange color), $\rho_{L8_{hypP_{i=1}}}$ (grey color), $\rho_{L8_{hypP_{mult}}}$ (purple color), and absolute difference between $\rho_{L8_{i=1}}$ and $\rho_{L8_{hypP_{mult}}}$ (red colored). It can be observed there is a discrepancy of 0.0106 TOA reflectance between the $\rho_{L8_{i=1}}$ and $\rho_{L8_{hypP_{mult}}}$. It might be because of EO-1 Hyperion's different band-to-band attributes in their relative domain. This small offset can further be minimized by finding the relative gain and performing relative calibration on the Hyperion sensor, which brings the satellite (L8 and S2A) hyperspectral profile to match its multispectral domain.

2.3.2 Relative Calibration on EO-1 Sensor

In the relative calibration process, the ratios between satellite measurements (ρ_{L8_i} and ρ_{S2A_k}) and the band-integrated TOA reflectance ($\rho_{L8_{hypP_{mult}}}$ and $\rho_{S2A_{hypP_{mult}}}$) are first

calculated. Then, the mean ratio across the central wavelengths is taken for L8, and S2A, called "relative gain" values.
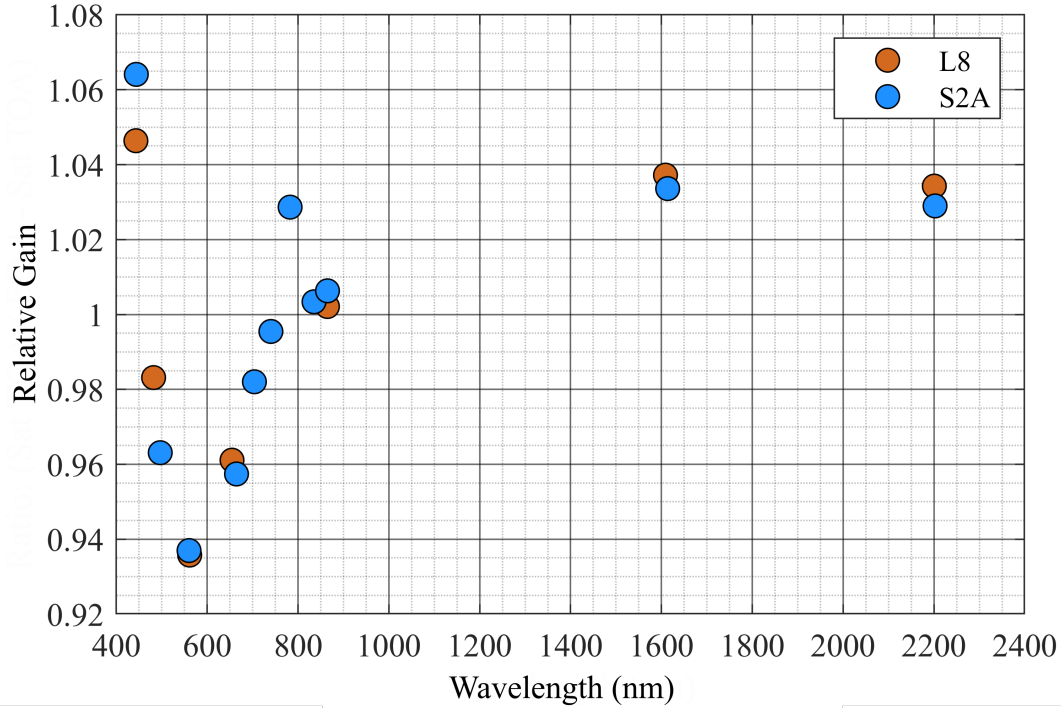
Figure 2.10. Relative gain for L8 and S2A vs the central wavelength.

Fig. 2.10 shows the relative gain for L8 (orange color) and S2A (blue color) versus the central wavelength. The relative gain values for L8 and S2A are combined to be "superspectral relative gain" values (orange color) as shown in Fig. 2.11. In order to obtain "hyperspectral relative gain" values, Modified Akima Cubic Hermite Interpolation (makima) interpolation is applied to the superspectral relative gains. The interpolated values can be obtained based on a piecewise function of polynomials with at most three degrees which is the advantage of using the 'makima' approach [38]. The interpolation is employed separately for VNIR and SWIR channels due to two sensors onboard Hyperion. Before employing the interpolation on the VNIR channel, the average relative gain between L8 and

S2A is taken for the 'green', 'red', and 'NIR' bands because they are very close to each other. Then the interpolation is performed to obtain interpolated relative gain values with 1 nm spectral resolution for VNIR channels. Similarly, for the SWIR channels, the average relative gain of L8 and S2A is computed and taken as a relative gain with 1 nm spectral resolution. The interpolated relative gain for VNIR and SWIR channels is further extrapolated and combined in order to cover the entire hyperspectral wavelength region. The EO-1 sensor used in this study has a hyperspectral TOA reflectance profile with a 10 nm spectral resolution. In order to match with the EO-1 sensor resolution, the combined interpolated relative gain values are integrated to obtain a 10 nm resolution of hyperspectral relative gain values.
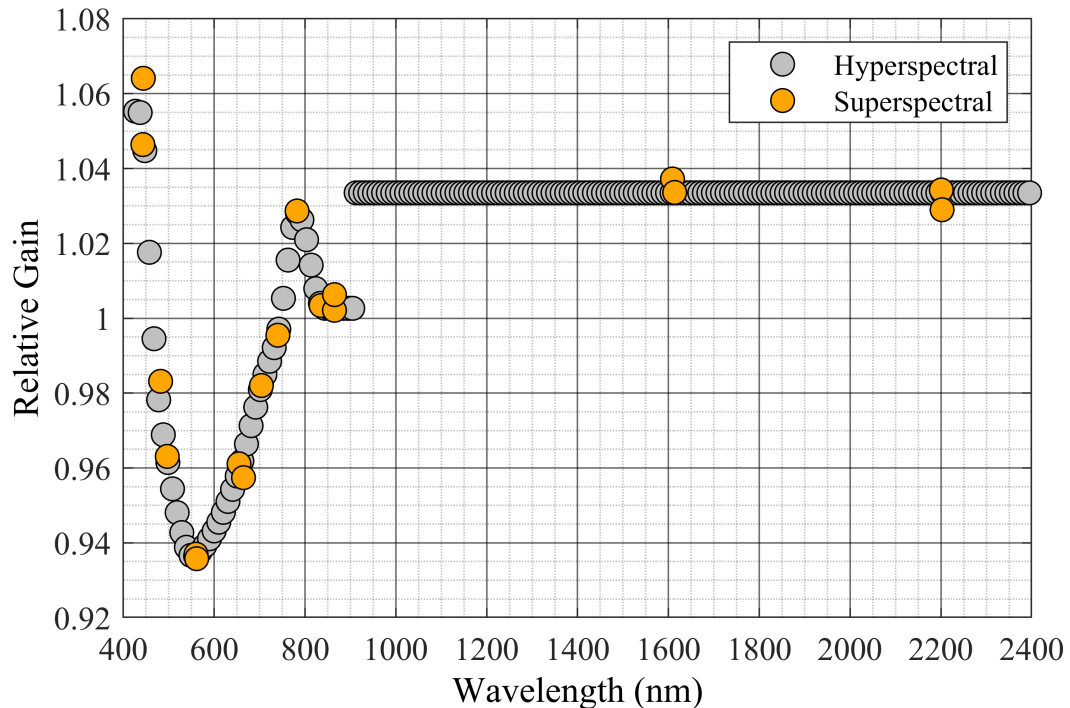
Figure 2.11. Superspectral and hyperspectral (for calibrated Hyperion wavelengths) relative gain.
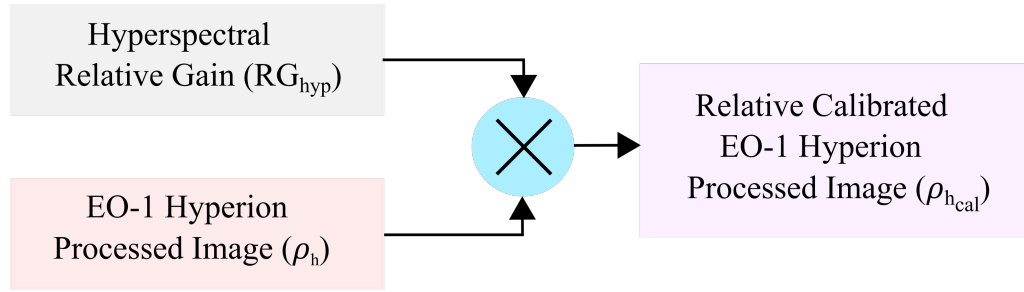
Figure 2.12. Block diagram showing the relative calibration on EO-1 Hyperion processed image.

Fig. 2.11 shows the hyperspectral (grey color) and superspectral (orange-colored) relative gain plot. Finally, the hyperspectral relative gain is multiplied with the TOA reflectance of the 64 Hyperion processed images ($\rho_{h_{j=1..N}}$), which completes the relative calibration on the EO-1 sensor as shown in Fig.2.12. The output of the relative calibration process, which is the relative calibrated EO-1 Hyperion processed image ($\rho_{h_{cal}}$), is used as an input parameter for "Input 2" in Fig. 2.7.

2.3.3 Normalized Hyperspectral Profile after Relative Calibration

The processed image information for L8 (ρ_{L8}), S2A (ρ_{S2A}), and relative calibrated EO-1 Hyperion processed image information ($\rho_{h_{cal}}$) form a new input data called "Input 2". Input 2 shown in Fig. 2.7 is now used in the multispectral to hyperspectral profile conversion for L8 and S2A following the same procedures illustrated in Fig. 2.8, explained in Section 2.3.1. The normalized hyperspectral profile obtained from the conversion process using "Input 2" is then compared with their satellite measurements. Fig 2.13 shows the L8 normalized hyperspectral profile, $\rho_{L8_{hyp}}$ (grey color) along with its band integrated multispectral form $\rho_{L8_{hyp_{mult}}}$ (purple circle). The orange circle represents the observed TOA reflectance ($\rho_{L8_{i=1}}$). The absolute difference (red bar) is calculated between $\rho_{L8_{i=1}}$ and band-integrated multispectral TOA reflectance ($\rho_{L8_{hyp_{mult}}}$) as shown in Fig 2.13. It can be

concluded that performing the relative calibration on the EO-1 sensor reduces the offset and the hyperspectral profile highly matches with its observed multispectral domain.
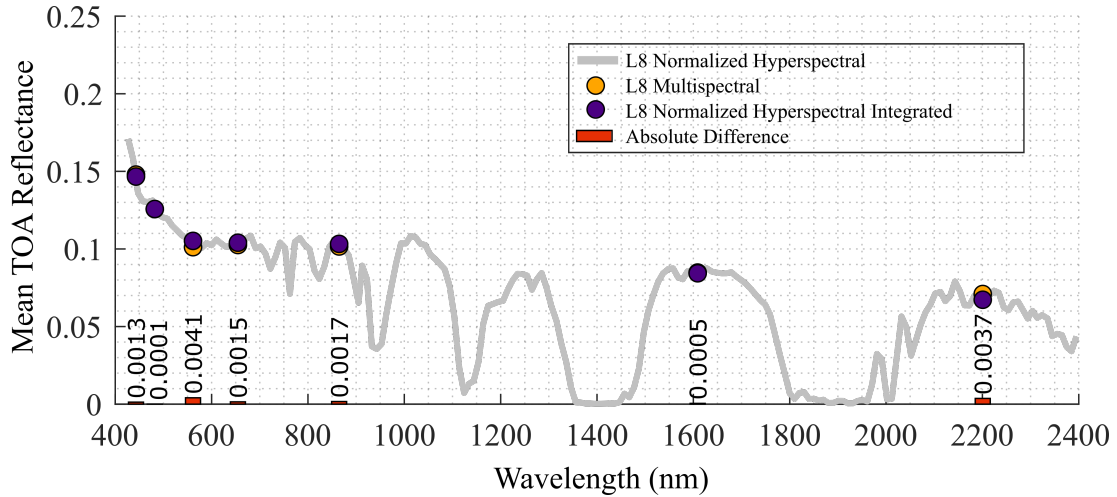
Figure 2.13. Showing L8 normalized hyperspectral TOA reflectance (grey curve), L8 multispectral TOA reflectance (orange circle), L8 normalized hyperspectral integrated TOA reflectance (purple circle), and absolute difference (red bar): after relative calibration.

There are *M* and *N* numbers of hyperspectral profile for L8 ($\rho_{L8_{hyp}}$) and S2A ($\rho_{S2A_{hyp}}$) respectively. Fig. 2.14 shows L8 normalized hyperspectral profile (gray color), L8 measurements (orange circle), and the relative calibrated Hyperion profile (blue color). The S2A normalized hyperspectral profile (grey color), S2A measurements (orange circle), and the relative calibrated Hyperion profile (blue color) are shown in Fig. 2.15. It can be observed that ρ_{L8} and ρ_{S2A} align within the range of normalized hyperspectral profile for both L8 and S2A sensors. It can also be justified that the normalized hyperspectral profile obtained in this process truly represents satellite data in the multispectral domain.
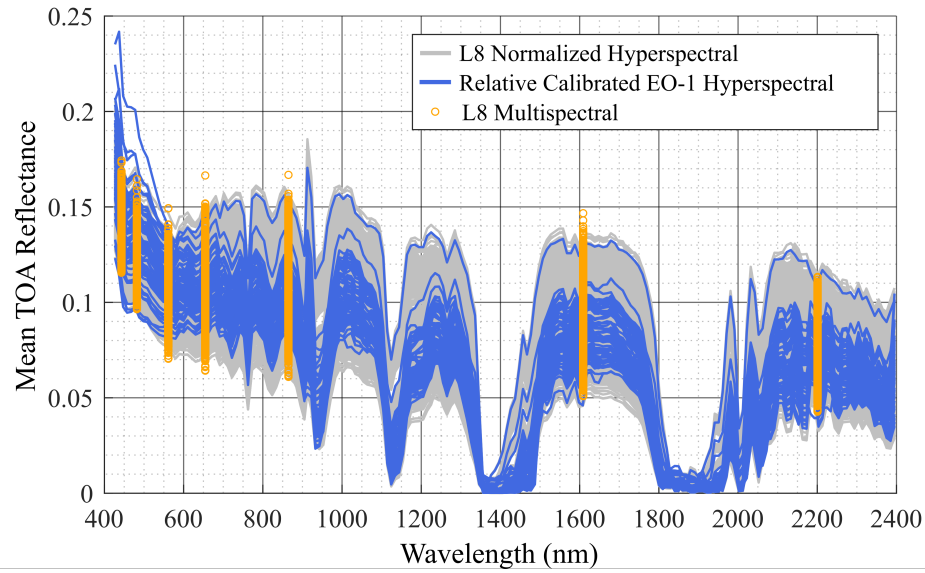
Figure 2.14. L8 normalized hyperspectral TOA reflectance (grey line), EO-1 hyperspectral TOA reflectance after relative gain correction (blue line) and, L8 multispectral TOA reflectance (orange circle).
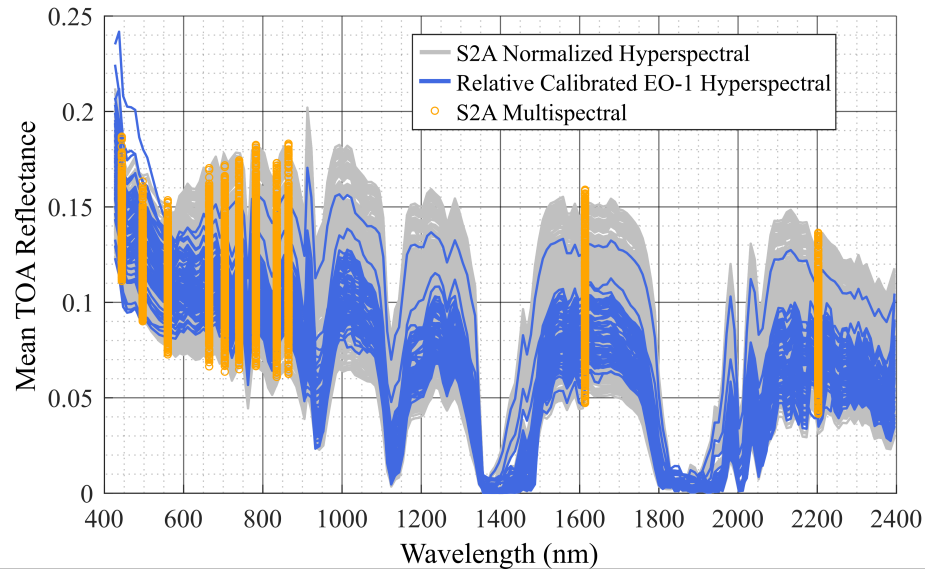
Figure 2.15. S2A normalized hyperspectral TOA reflectance (grey line), EO-1 hyperspectral TOA reflectance after relative gain correction (blue line), and S2A multispectral TOA reflectance (orange circle).

The DaHD consists of a combination of L8 and S2A normalized hyperspectral

profiles, a total of 1925 (M = 1150, N =775) profiles. The DaHD consisting of reflectance

measurements in the range of 0.04 – 0.2, will then be used to develop the DAHAC model.

2.4   Dark Hyperspectral Absolute Calibration Model Development

2.4.1   4 Angle Hyperspectral BRDF Model

Since the Earth's surface is the non-Lambertian target, solar illumination, and sensor viewing geometry can significantly impact the TOA reflectance of a given target. Most often, the BRDF can be used to model this effect [1]. In this study, the DaHD is used to develop the 4 angle hyperspectral BRDF model. During this process, the spherical angle associated with the DaHD viz; solar zenith angle (SZA) ranging from $15° – 60°$, solar azimuth angle (SAA) from $31° – 163°$, view zenith angle (VZA) from $0.03° – 10°$, and view azimuth angle (VAA) from $-177° – 180°$ are converted into the Cartesian coordinates form using Eq. (2.7), (2.8), (2.9) and (2.10), respectively.

$$Y_1 = sin(SZA) \times cos(SAA) \tag{2.7}$$

$$X_1 = sin(SZA) \times sin(SAA) \tag{2.8}$$

$$Y_2 = sin(VZA) \times cos(VAA) \tag{2.9}$$

$$X_2 = sin(VZA) \times sin(VAA) \tag{2.10}$$

where X_1 and Y_1 represents Cartesian coordinates obtained using SZA and SAA, while X_2 and Y_2 represent Cartesian coordinates obtained using VZA and VAA.
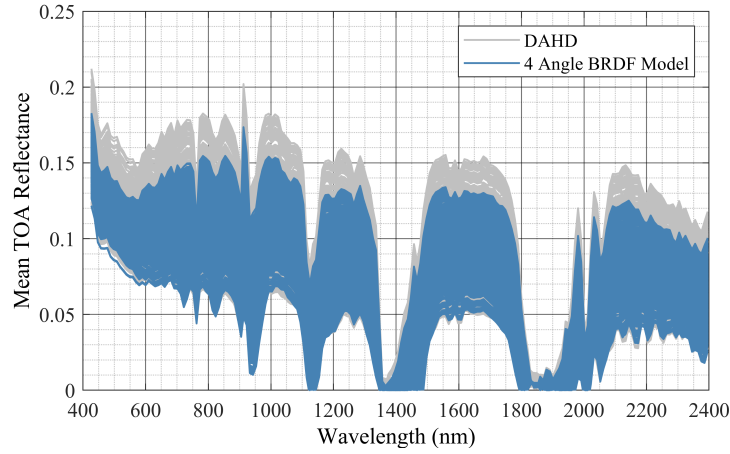
Figure 2.16. Dark hyperspectral dataset (grey) vs 4 angle hyperspectral BRDF model predicted TOA reflectance profile (blue).
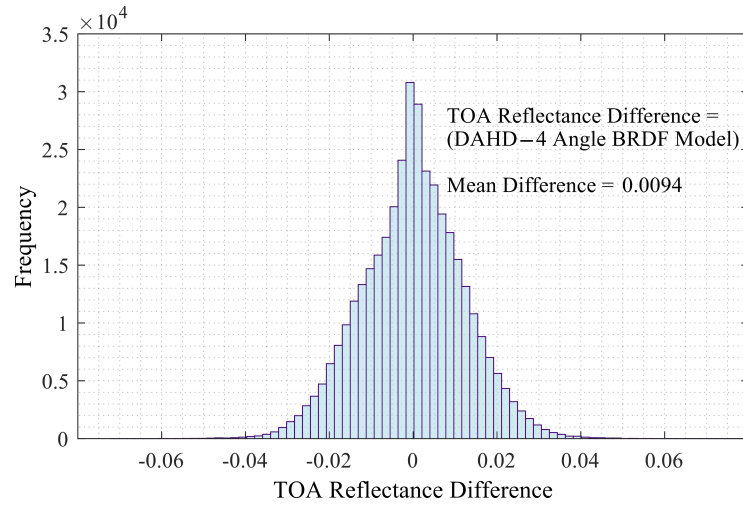
Figure 2.17. TOA reflectance differences between DaHD vs 4 angle hyperspectral BRDF model for 196 bands.

In order to achieve symmetry with regard to the scattering plane and to provide a robust fit to the 4 angle hyperspectral BRDF model, the DaHD along with their angular information in the converted Cartesian coordinates are then mirrored to each quadrant. Consequently, the TOA reflectance becomes a continuous function of independent variables [22]. Using the new set of the independent variables in the Cartesian coordinates form (X_1, Y_1, X_2, Y_2) and the mirrored DaHD, the 4 angle multi-quadratic least-squares regression

model is derived as shown in Eq. (2.11). It is important to note that, the 4 angle

hyperspectral BRDF model developed in this study utilizes all the DaHD imagery data to

cover the entire angular information.

$$
\begin{aligned}
\rho\left(\lambda, X_1, Y_1, X_2, Y_2\right) = & \beta_0 + \beta_1 X_1(\lambda) + \beta_2 Y_1(\lambda) + \beta_3 X_2(\lambda) + \beta_4 Y_2(\lambda) + \beta_5 X_1 Y_1(\lambda) \\
& + \beta_6 X_1 X_2(\lambda) + \beta_7 X_1 Y_2(\lambda) + \beta_8 Y_1 X_2(\lambda) + \beta_9 Y_1 Y_2(\lambda) + \beta_{10} X_2 Y_2(\lambda) \\
& + \beta_{11} X_1^2(\lambda) + \beta_{12} Y_1^2(\lambda) + \beta_{13} X_2^2(\lambda) + \beta_{14} Y_2^2(\lambda)
\end{aligned}
$$

$$(2.11)$$

Where ρ is the predicted TOA reflectance with respect to wavelength (λ) and 4 angle

Cartesian coordinates (X_1, Y_1, X_2, Y_2). β_0 represents the BRDF intercept, and the 14 BRDF

model coefficients $\beta_1, \beta_2, \beta_3, \beta_4, \beta_5, \beta_6, \beta_7, \beta_8, \beta_9, \beta_{10}, \beta_{11}, \beta_{12}, \beta_{13},$ and β_{14} represent

quadratic and linear coefficients.

Once the 4 angle BRDF model is developed, the predicted TOA reflectance is

compared against DaHD shown in Fig. 2.16. The TOA reflectance difference is calculated

between the DaHD profile and the predicted 4 angle BRDF Model to determine the level of

agreement between them. The distribution of TOA reflectance differences for all 196 bands

is shown in the histogram in Fig. 2.17. It can be observed that the TOA reflectance

difference is normally distributed and the majority of the difference lies within 0.02 TOA

reflectance for all 196 hyperspectral bands.

2.4.2   Dark Hyperspectral Absolute Calibration (DAHAC) Model

In order to develop the DAHAC model, a hypothesis test is applied to all 15 BRDF

model coefficients at the 95% significance level for all 196 hyperspectral bands. The

hypothesis test results (model coefficients, estimate, standard error, t-statistics values,

p-values, and each coefficient statistical significance) for the band with 864 nm wavelength
are summarized in Table. 2.3.

Table 2.3. Showing 4 angle hyperspectral BRDF model coefficients for 864 nm wavelength.

Coefficient	Estimate	Standard Error	T-Statistics	P-Value	Statistical Response
Intercept	0.14	6e-04	226.20	0	Significant
X_1	-7.59e-18	3.30e-04	-2.3e-14	1.0	Insignificant
Y_1	-2.71e-17	3.88e-04	-6.98e-14	1.0	Insignificant
X_2	7.33e-18	0.006	1.18e-15	1.0	Insignificant
Y_2	1.50e-18	0.002	7.64e-16	1.0	Insignificant
X_1Y_1	3.24e-18	9.59e-04	3.38e-15	1.0	Insignificant
X_1X_2	0.16	0.02	9.08	1.27e-19	Significant
X_1Y_2	-4.67e-17	0.005	-8.7e-15	1.0	Insignificant
Y_1X_2	2.79e-17	0.02	1.27e-15	1.0	Insignificant
Y_1Y_2	0.16	0.007	22.32	5.42e-107	Significant
X_2Y_2	2.45e-18	0.05	4.58e-17	1.0	Insignificant
X_1^2	-0.08	8.13e-04	-107.41	0	Significant
Y_1^2	-0.06	0.003	-19.69	2.75e-84	Significant
X_2^2	16.97	0.48	-35.29	4.32e-253	Significant
Y_2^2	1.62	0.04	36.63	5.69e-271	Significant

All of the Hyperion bands are validated by this statistical analysis, excluding a few
bands at 942 nm and 1386 nm, which represent water vapor and cirrus with high absorption
features. The p-value for the t-statistic hypothesis evaluated whether or not the BRDF
coefficients are equal to zero. When the p-value exceeds 0.05, the corresponding BRDF
coefficient becomes insignificant and vice versa. There are only the seven significant
coefficients viz; X_1X_2, Y_1Y_2, X_1^2, Y_1^2, X_2^2, Y_2^2 and the intercept as shown in Table. 2.3. They
are used to represent the DAHAC model. It is important to note that the atmospheric
parameters are not considered when developing the model in this study since they have a
negligible effect on the atmospheric model and the absolute calibration model [39]. The
DAHAC model with seven coefficients is derived using the solar zenith and azimuth angles

and sensor zenith and azimuth angles as shown in Eq. 2.12 below:

$$\rho(\lambda, X_1, Y_1, X_2, Y_2)_{DAHAC} = B_0(\lambda) + B_1(\lambda)X_1X_2 + B_2(\lambda)Y_1Y_2 + B_3(\lambda)X_1^2 +$$

$$B_4(\lambda)Y_1^2 + B_5(\lambda)X_2^2 + B_6(\lambda)Y_2^2$$

(2.12)

Where, $\rho_{(\lambda, X_1, Y_1, X_2, Y_2)_{DAHAC}}$ is the model predicted TOA reflectance with respect to

wavelength (λ) and the Cartesian coordinates (X_1, Y_1, X_2, Y_2). The predicted TOA reflectance

has a spectral resolution of $10nm$. B_0 represents the intercept, and B_1, B_2, B_3, B_4, B_5, and B_6

are the model coefficients corresponding to X_1X_2, Y_1Y_2, X_1^2, Y_1^2, X_2^2, and Y_2^2, respectively.

Unlike the hyperspectral model developed by Chaity et al. [1], it should be noted

that the DAHAC model does not require any adjustment factor in the model equation to

scale the Hyperion spectrum due to low reflectance in all bands. The DAHAC model

coefficient values for 196 hyperspectral bands are shown in Fig. 2.18.

The validation of the DAHAC model (7 Coefficients) with 4 angle hyperspectral

BRDF model (15 Coefficients) for all hyperspectral bands is shown in Fig. 2.19 (a). It can

be observed that the plot shows a linear behavior which means the DAHAC model

statistically agrees with the 4 angle hyperspectral BRDF model with a slope equal to one

and bias close to zero. Fig. 2.19 (b) shows the TOA reflectance differences between the two

models, and the mean absolute error (MAE) calculated using Eq. 2.13 is found to be close

to zero. This provides significant evidence that the DAHAC model is capable of predicting

the DaHD. The DAHAC model will be further validated with Landsat missions and

Sentinel-2 missions in Section 3.
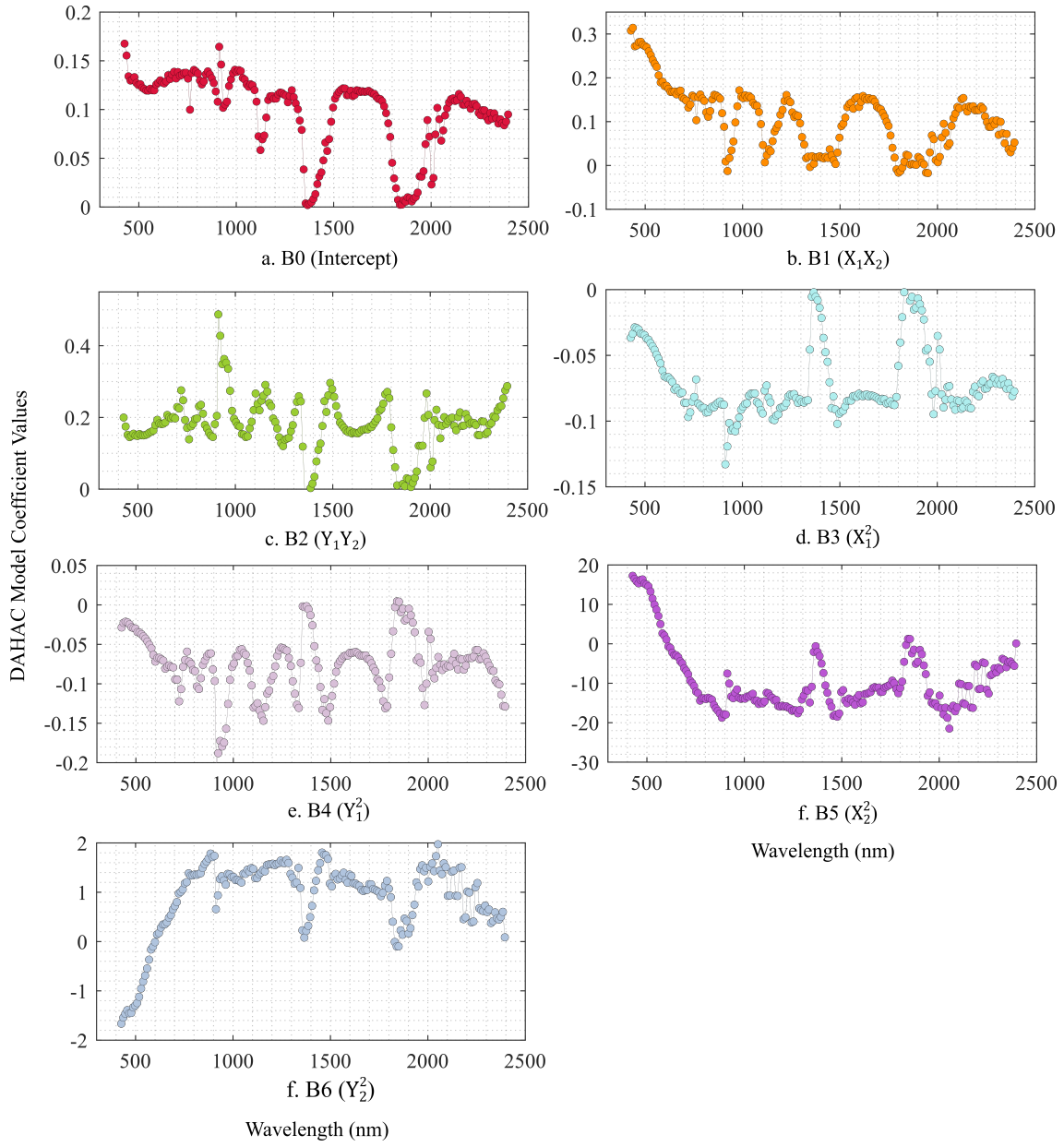
Figure 2.18. DAHAC model coefficients values for 196 hyperspectral bands.

$$MAE = \frac{\sum_{j=1}^{n} |y_j - \hat{y}_j|}{n} \tag{2.13}$$

Where, y_j: 4 angle hyperspectral BRDF Model predicted TOA reflectance, $\hat{y}_j$: DAHAC
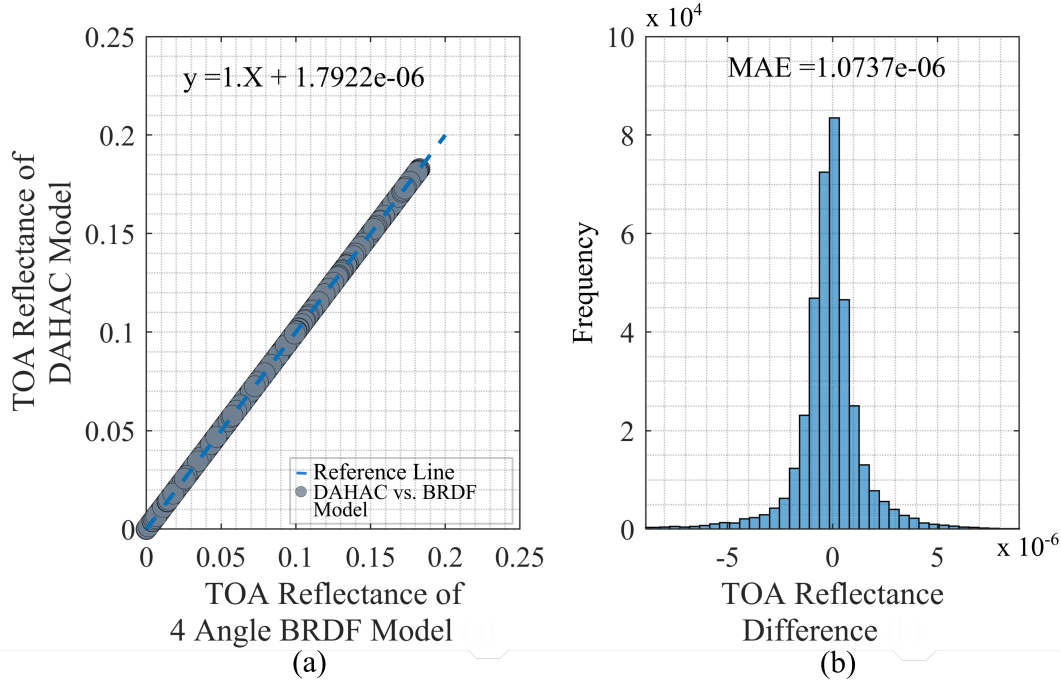
Figure 2.19. Showing (a) TOA Reflectance of 4 angle hyperspectral BRDF model (15 Coefficients) vs. DAHAC Model (7 Coefficients) and (b) Histogram with TOA reflectance difference between 4 angle hyperspectral BRDF model vs. DAHAC model TOA reflectance.

Model predicted TOA reflectance and n: number of hyperspectral bands. The model performance is evaluated using two metrics: accuracy and precision in unit reflectance due to low reflectance target. Accuracy and precision are measured by calculating the mean, and standard deviation of differences between the satellite observed and model predicted TOA reflectance using Eq.2.14 and Eq. 2.15, respectively.

$$Accuracy = mean(\rho_{sat} - \rho_{model}) \tag{2.14}$$

$$Precision = std(\rho_{sat} - \rho_{model}) \tag{2.15}$$

where, ρ_{sat} refers to satellite observed TOA reflectance, and ρ_{model} represents the DAHAC model predicted TOA reflectance i.e. $\rho(\lambda, X_1, Y_1, X_2, Y_2)_{DAHAC}$.

CHAPTER 3   RESULTS AND DISCUSSION

In this section, the results of the model validation to determine the model accuracy with respect to different sensors are presented and analyzed.

3.1   DAHAC Model Validation Process

In order to evaluate the DAHAC model performance and its accuracy, it is validated with five different sensors viz; L7, L8, L9, S2A, and S2B. During the validation process, the spherical angular information (SZA, SAA, VZA, and VAA) are first transformed into the Cartesian coordinates form for each sensor (L7, L8, L9, S2A, and S2B). Using the converted Cartesian coordinates and the DAHAC model coefficients shown in Fig. 2.18 as the input parameters for the DAHAC model, the hyperspectral TOA reflectance is predicted for each sensor. The hyperspectral TOA reflectance response from the model has a 10 nm resolution which is then subjected to cubic interpolation to obtain a finer $1nm$ spectral resolution. Since multispectral sensors are used for validation in this study, the RSR of each sensor is then used to integrate the interpolated hyperspectral TOA reflectance into the multispectral TOA reflectance. Finally, the model response in the form of multispectral TOA reflectance is compared with the observed TOA reflectance of each sensor used for validation purposes. The results from the DAHAC model validation for L7, L8, L9, S2A, and S2B are presented in the following subsections:

3.1.1   DAHAC Model Validation with Landsat Missions

The DAHAC model predicted, and the observed L8 TOA reflectance for seven bands are compared with respect to decimal year and SZA as shown in Fig. 3.1 (a)-(g).

The left-hand side plots with respect to the decimal year showing seasonal variation
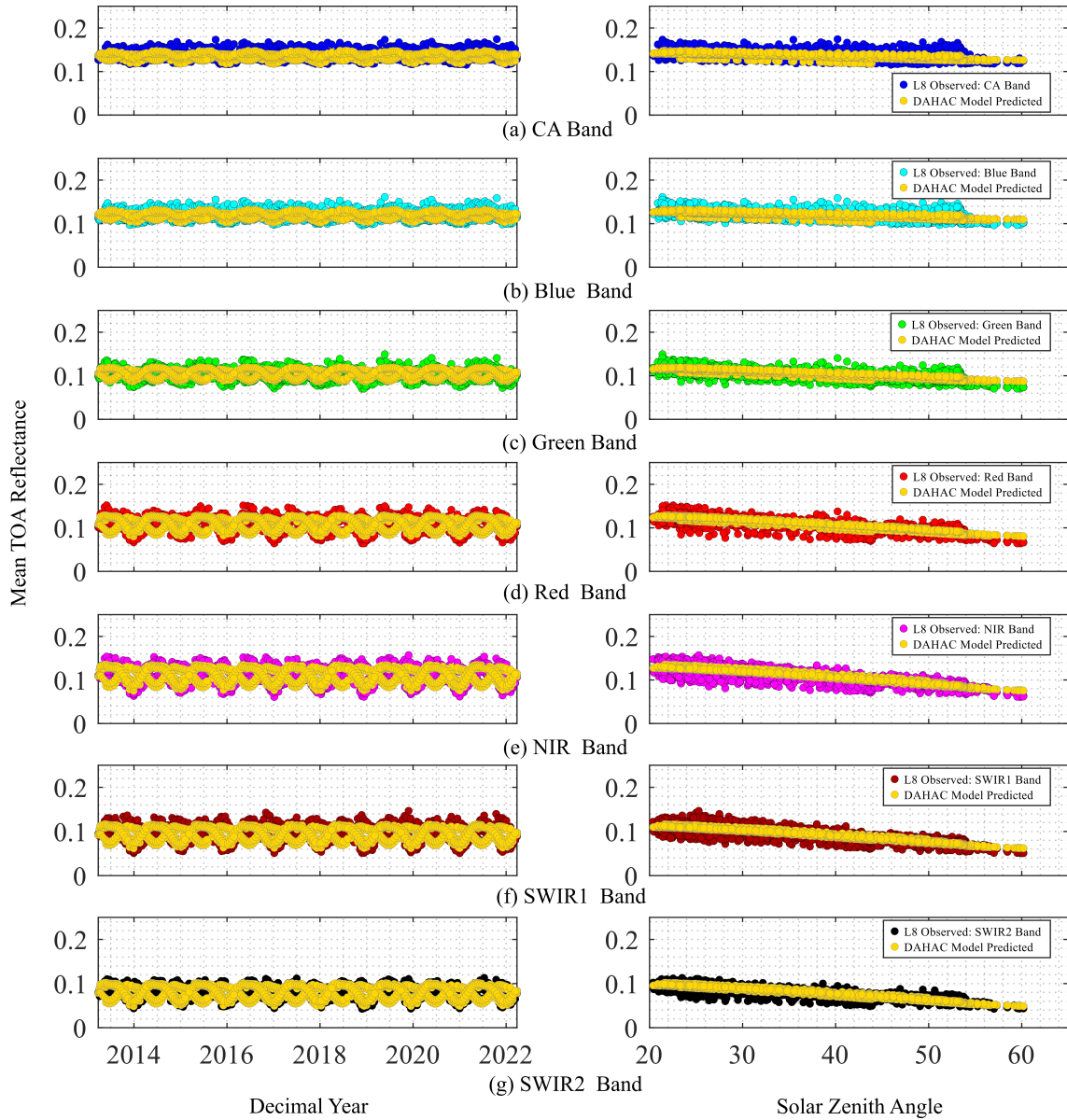
Figure 3.1. DAHAC model validation on L8 across seven spectral bands.

and well-captured by the model for every band. The right-hand side plots show the decreasing linear trend of the observed TOA reflectance with respect to SZA, the DAHAC model predicted TOA reflectance is well agreed with L8 measurements for all spectral bands.

The performance of the DAHAC model on Landsat sensors (L7, L8, and L9) is evaluated by measuring the difference between the observed TOA reflectance of Landsat

Figure 3.2. TOA reflectance difference between Landsats observed TOA reflectance and the DAHAC model response across seven spectral bands, showing mean TOA reflectance difference and standard deviation (pink).

sensors with the DAHAC model response. The error distribution for L7, L8, and L9 across the bands are further shown in the violin plot as illustrated in Fig. 3.2 (a), (b), and (c), respectively. The error bar in each violin plot shows the mean and 1σ standard deviation of the TOA reflectance difference. It is clearly seen from the violin distribution in Fig. 3.2 (a)-(c) that for all three Landsat sensors (L7, L8, L9), the majority of TOA reflectance difference falls within ± 0.02 for all spectral bands. The average mean difference ranges between 0 and 0.012 for all bands.

3.1.2   DAHAC Model Validation with Sentinel-2 Missions

The DAHAC model validation process for Sentinel-2 missions is the same as the

Landsat missions. Fig. 3.3 shows the comparison between the predicted TOA reflectance

and observed S2A measurements for non-Landsat bands (Red-Edge1, Red-Edge2,

Red-Edge3, NIR1) with respect to decimal year and SZA. It can be observed that seasonal

variation in the Sentinel measurements matches very well with the DAHAC model

predicted TOA reflectance for all non-Landsat bands. Fig. 3.4 (a) and (b) shows the

majority of the TOA reflectance difference falls within ±0.02 TOA reflectance for

Sentinel-2 missions (S2A, S2B). The average mean difference ranges within 0-0.004 TOA

reflectance for all spectral bands.

The hyperspectral BRDF model developed in [1] depends on the hyperspectral

cross-scale factor to normalize the Hyperion intercept spectral profile for different spectral

bands. The advantage of using the DAHAC model is that it will be independent of

calculating and estimating the adjustment factors for scaling the Hyperion spectrum. The

dark target data is obtained from all three sensors (L8, S2A, and EO-1) in the range of 0.04 –

0.2 TOA reflectance for all spectral bands used for the DAHAC model development.

Following the DAHAC model specifications for solar zenith angle ($15° – 60°$), solar

azimuth angle ($31° – 163°$), view zenith angle ($0.03° – 10°$), and view azimuth angle ($-177°$

$– 180°$), the predicted results showed that the model is able to estimate the TOA reflectance

measurements with the highest accuracy of ±0.012 and precision within 0.02 unit

reflectance for all Landsat satellites spectral bands.

The model performance for Sentinel sensors (S2A and S2B) showed accuracy and
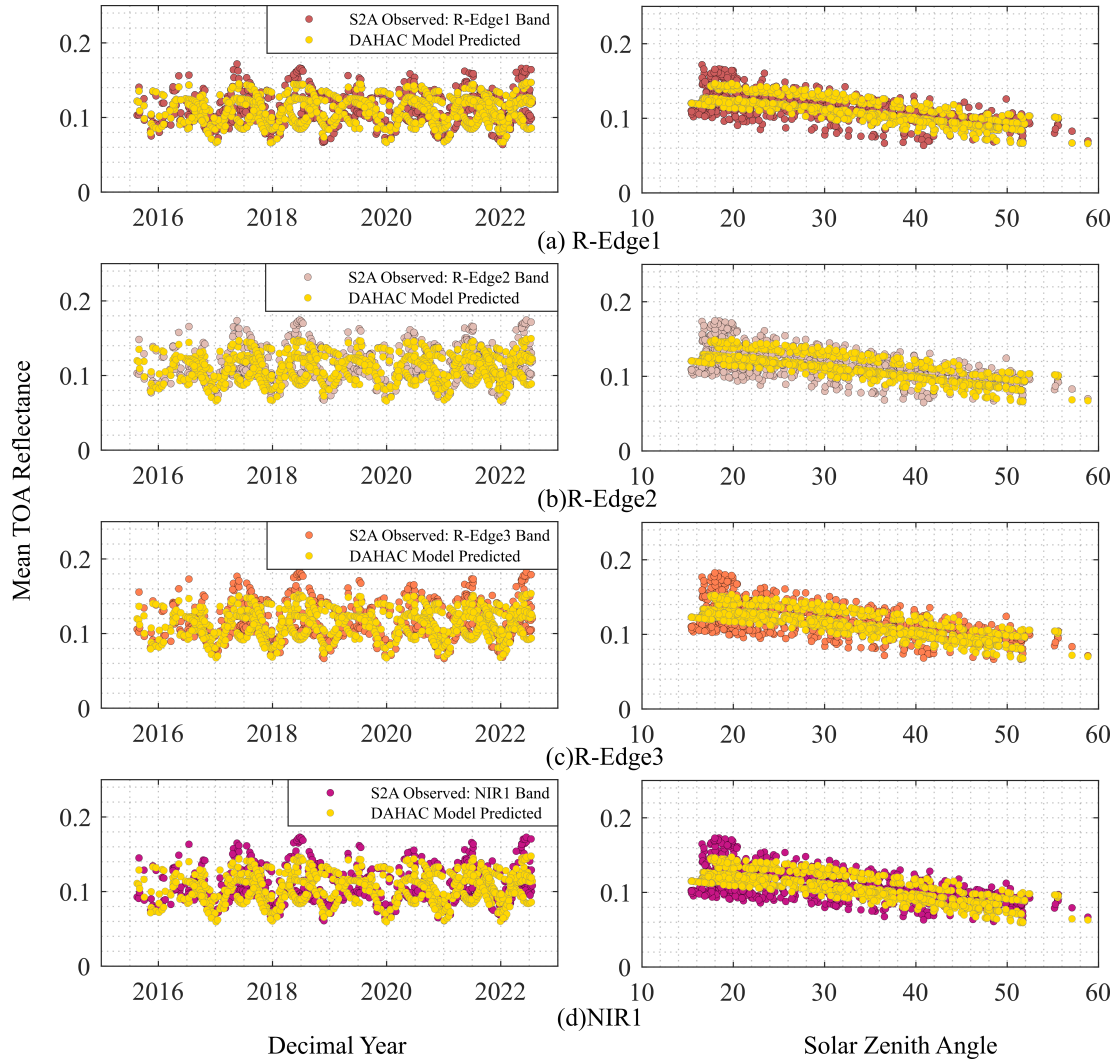
Figure 3.3. DAHAC Model validation on S2A for non-Landsat bands.

precision within ± 0.004 and ± 0.02 unit reflectance. Additionally, the TOA reflectance predicted using the DAHAC model has a 10 nm spectral resolution, and a finer 1 nm resolution is then obtained by further subjecting the model to cubic interpolation.
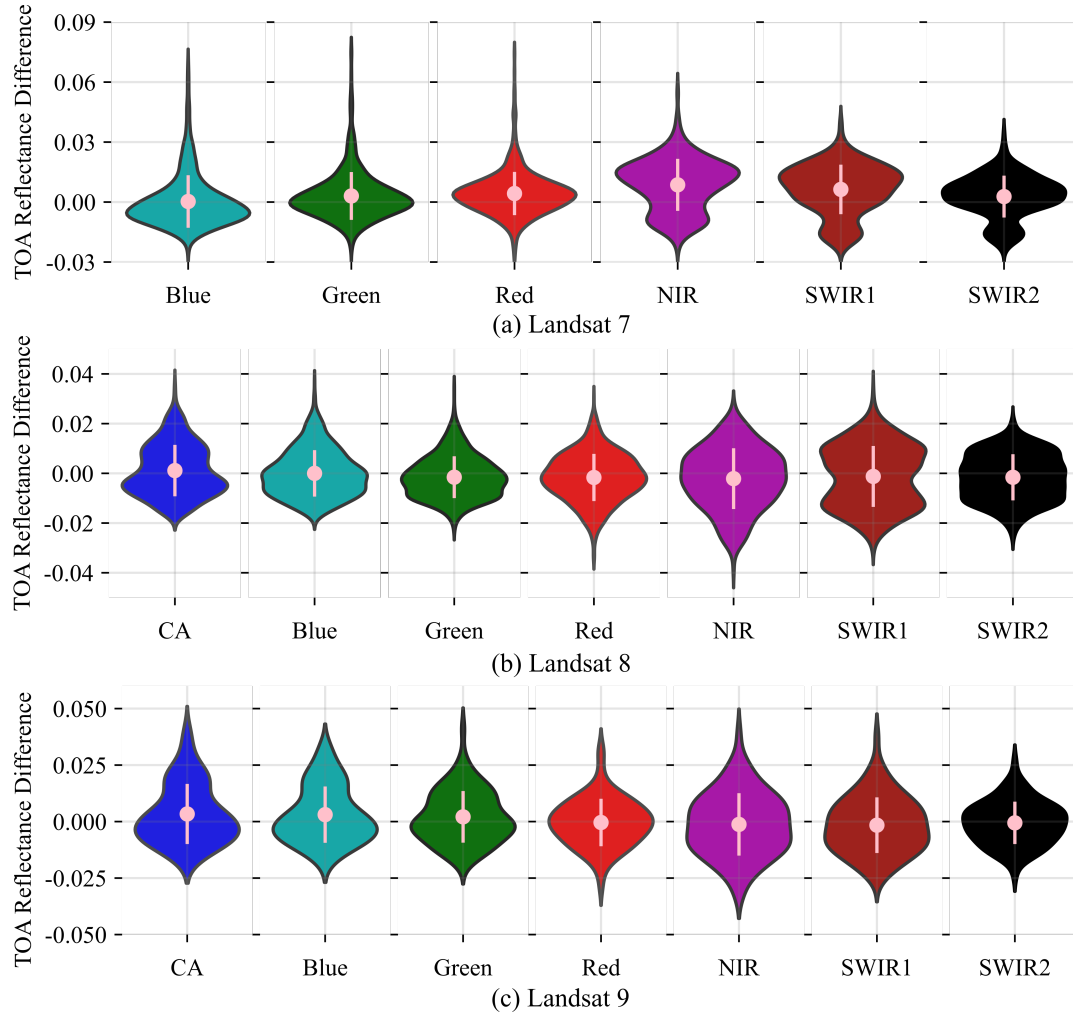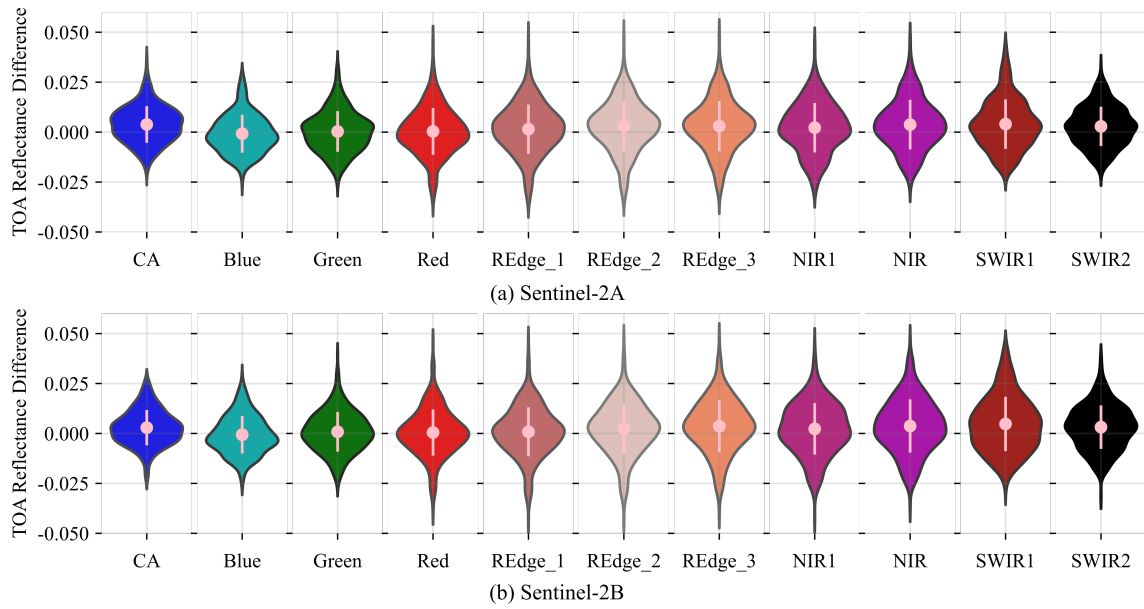
Figure 3.4. TOA reflectance difference between S2A observed information and the DAHAC model response across eleven spectral bands.

This implies that the DAHAC model can perform absolute calibration of any sensor over the dark EPICS-Global with a 1 nm spectral resolution.

CHAPTER 4   UNCERTAINTY ANALYSIS

In this section, the uncertainty analysis for the DAHAC model is performed. The sensors viz; L8, S2A, and EO-1 Hyperion used for the DAHAC model development have currently been determined to have uncertainties at 2% [7], 4% [39], and 5% − 10 % [35], respectively. It is initially assumed that the DAHAC model's uncertainty relates to the uncertainty on the relative calibration of the EO-1 sensor, all the steps involved in the model development, the DaHD generation process, and development of the BRDF model as described in Section 2.3, and 2.4.
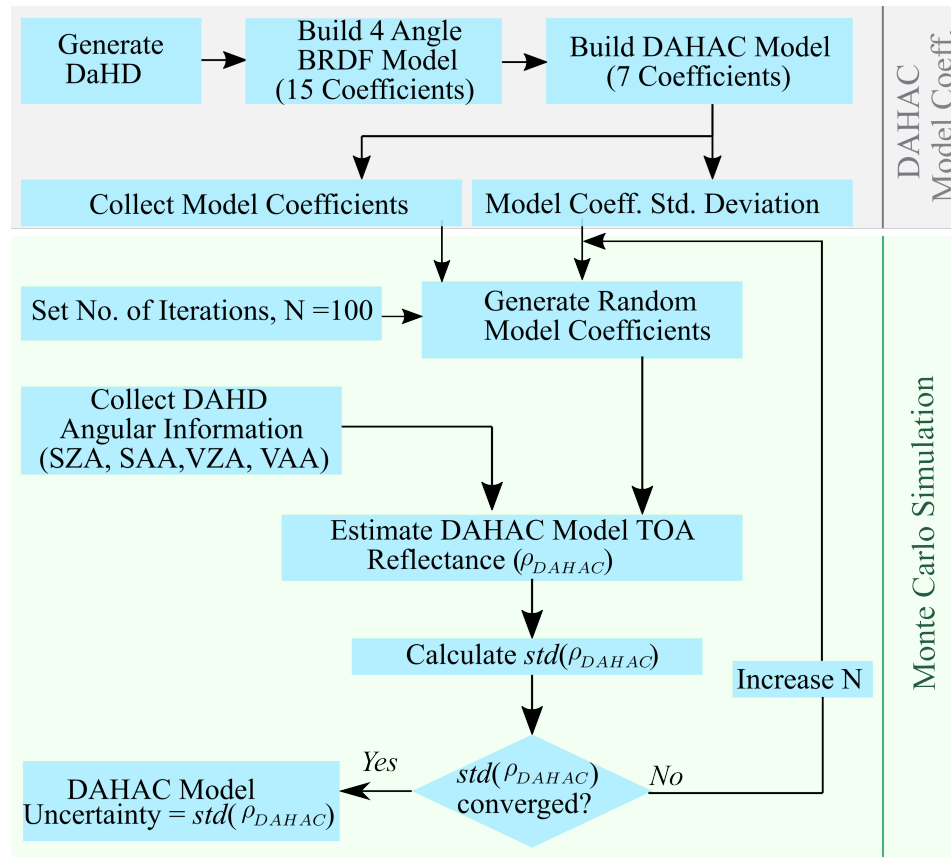
Figure 4.1. Flowchart showing the calculation of DAHAC model uncertainty.

The flowchart shown in Fig. 4.1 illustrates the steps followed in the DAHAC model uncertainty calculation. The standard deviation for coefficient estimates of the DAHAC model is calculated using the formula: $Coeff_{std} = \frac{CI_U - CI_L}{2 \times t-value}$, where CI_U and CI_L represent the upper bound and lower bound of confidence interval (CI), respectively and t-value corresponds to the 95% CI and degree of freedom. Monte Carlo simulation is then employed to generate multivariate normal random numbers for the model coefficients using the model coefficients and their standard deviation information with the number of iterations set to 100. Using the randomized model coefficients obtained from this simulation and angular information (SZA, SAA, VZA, VAA) from DaHD in Cartesian coordinates, the DAHAC model predicts the TOA reflectance at each iteration level. The standard deviation of the predicted TOA reflectance of the DAHAC model is then estimated for all 196 bands. The simulation is performed by increasing the number of iterations at different levels (100, 500, 1000, 1500, 2000, 2500) until the standard deviation of the predicted TOA reflectance of the DAHAC model has converged. Once the standard deviation is converged to a stationary point, the simulation stops, and the standard deviation at that point represents the DAHAC model uncertainty.
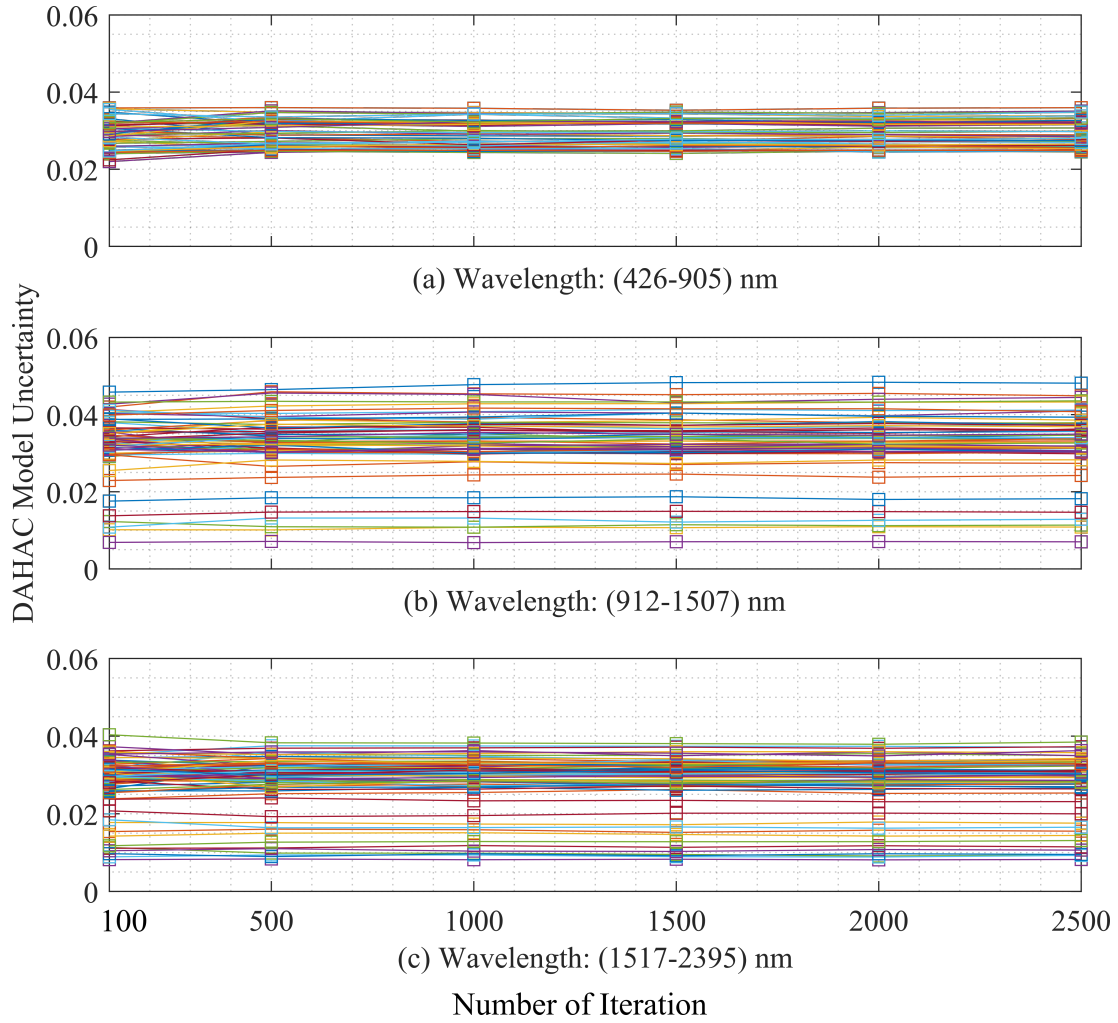
Figure 4.2. DAHAC model uncertainty using Monte Carlo simulation at different iteration levels (100 - 2500).

Fig. 4.2 shows the results of the standard deviation of the DAHAC model predicted TOA reflectance using the Monte Carlo simulation. The three plots in Fig. 4.2 (a), (b), and (c) represent different wavelength ranges: (426-905) nm, (912-1507) nm, and (1517-2395) nm, respectively. It can be observed that the standard deviation nearly converges between 1500 and 2500 iterations; the range is stable for all 196 bands. The uncertainty of the DAHAC model is then selected to be the model standard deviation at the 1500 iteration level. Fig. 4.3 shows the DAHAC model predicted TOA reflectance and the DAHAC model
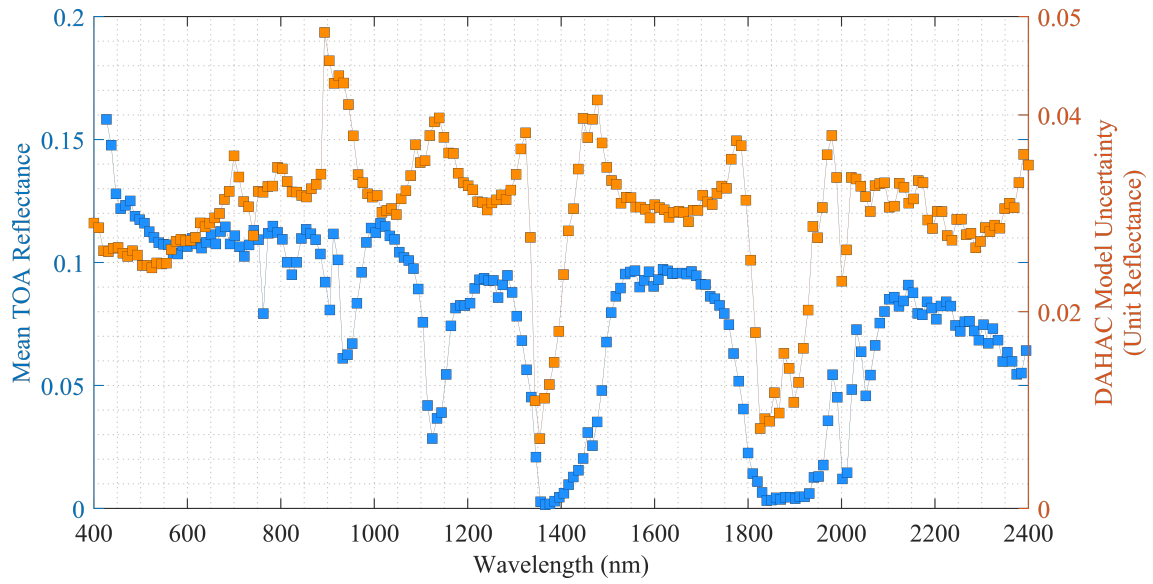
Figure 4.3. Mean TOA reflectance of the DAHAC model (blue colored), and DAHAC model uncertainty in unit reflectance (orange colored) for 426 nm-2395 nm wavelength range.

uncertainty associated with each hyperspectral band. This analysis shows that the model uncertainty for VNIR and SWIR channels is within 0.04 and 0.05 unit reflectance, respectively.

CHAPTER 5   THE DAHAC MODEL DOUBLE RATIO FOR SENSORS

INTER-COMPARISON

The ratio between the DAHAC model TOA reflectance and satellite measurements

is used to determine the DAHAC model double ratio. The DAHAC model double ratio is

used as a metric to perform the inter-comparison between two satellites across each spectral

band. The double ratio approach eliminates any possible bias or error that could be

embedded in the DAHAC model. Thus, it can be used as a transfer mechanism to directly

compare two satellites, for instance, L8 and L9, or S2A and S2B. During this process, the

ratio between model predicted TOA reflectance and observed TOA reflectance

measurements are calculated using Eq.5.1, termed as "Reflectance Ratio". Further, the

DAHAC model double ratio is calculated using Eq. 5.2.

$$\text{Reflectance Ratio}_{sat} = \frac{\text{DAHAC Model TOA Reflectance}}{\text{Observed TOA Reflectance}} \tag{5.1}$$

$$\text{DAHAC Model Double Ratio} = \frac{\text{Reflectance Ratio}_{sat}}{\text{Reflectance Ratio}_{ref}} \tag{5.2}$$

where "sat" refers to L8, L9, S2A, and S2B satellite sensors. "ref" represents the reference

sensors viz; L8 and S2A.

The image information from November 2021 to October 2022 is used to perform the

inter-comparison between L8 and L9. For S2A and S2B, the data for inter-comparison

analysis are taken from July 2017 to July 2022 over the dark target. In order to prevent the

study from being influenced by site variation resulting from various atmospheric conditions,
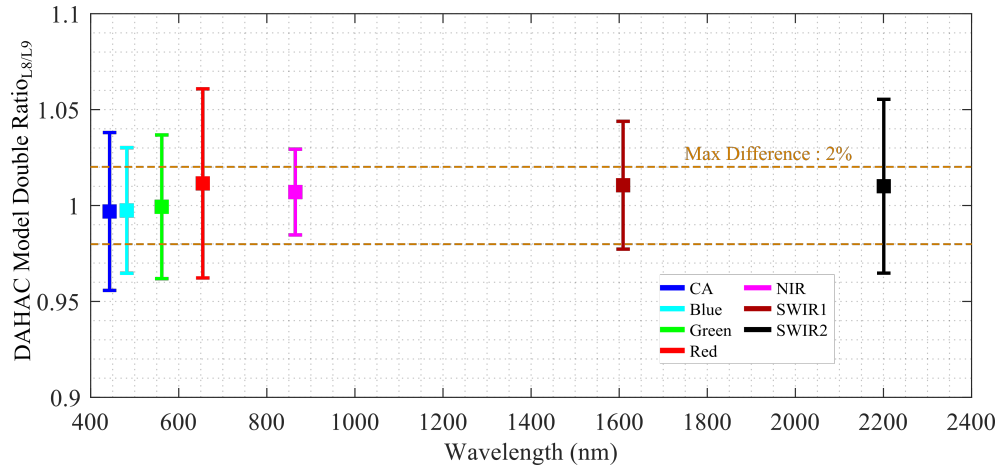
Figure 5.1. Double ratio between L8 and L9. Orange dotted lines shows maximum 2% differences between L8 and L9.
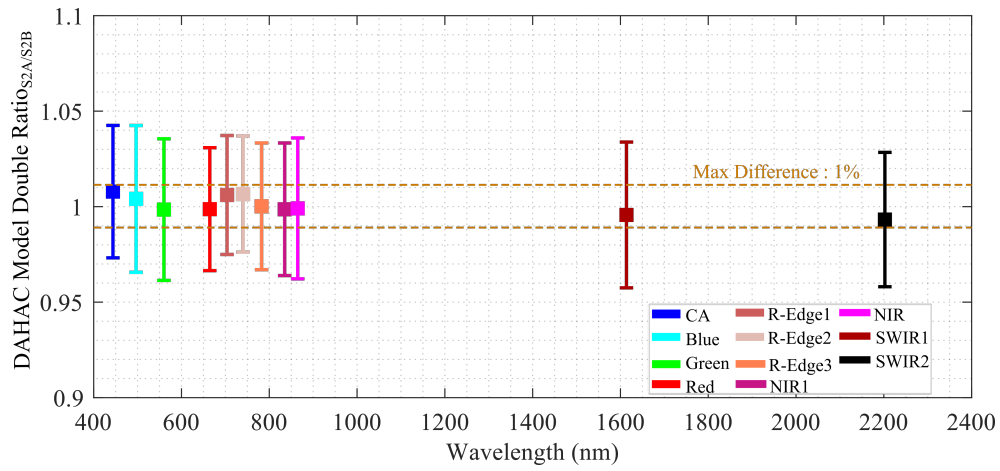
Figure 5.2. Double ratio between S2A and S2B. Orange dotted lines shows maximum 1% differences between S2A and S2B.

the image information is assumed to be stable within seven days. According to Gross et al., a smaller difference in the view zenith angle between two sensors leads to a reduced impact of several aspects of BRDF [40]. Using nearby coincident pairs within seven days with View Zenith Angle (VZA) difference less than $2°$, 46 and 617 pairs are obtained for L8 and L9, and S2A and S2B, respectively. The DAHAC model Double Ratio result shows that the L8 and L9 are comparable within 1% for all bands except for the Red band within 2% as shown in Fig.5.1. Sentinel-2A and 2B inter-comparison result shows the agreement within

1% for eleven spectral bands as shown in Fig. 5.2. In this way, a DAHAC model double

ratio helps to evaluate the measurement differences across each spectral band for different

sensors.

Being a part of the Landsat Cal/Val team, the SDSU IP Lab performed the

cross-calibration between L8 and L9, showing the agreement within 0.5% – 1% [41]. The

cross-calibration result between S2A and S2B was within ±2% over the Libya 4 site [42].

The DAHAC model double ratio gives similar results as reported in previous studies[15],

[23], [41]. It proves that the DAHAC model double ratio can be a complementary tool to be

used for satellite calibration.

CHAPTER 6   CONCLUSIONS

This paper presents the development of the novel DAHAC model using the normalized hyperspectral profile of L8 and S2A over Dark EPICS-Global. The Dark EPICS-Global includes different surface types viz; dark rock, volcanic area, and dark sand with a temporal variation of 0.02 unit reflectance as illustrated in Table. 2.2. The measurements of L8, S2A, and EO-1 Hyperion sensors were used to generate the dark hyperspectral data for the DAHAC model development. L8 and S2A are well-calibrated and used as reference sensors and the EO-1 Hyperion sensor as the hyperspectral library source. This study proposed an algorithm to obtain the normalized hyperspectral profile for L8 and S2A using the multispectral (L8, S2A) and hyperspectral (EO-1 Hyperion) domain data. The relative calibration of the EO-1 sensor significantly improved the agreement between the hyperspectral profile of L8 and S2A with its multispectral domain. The DaHD is generated by aggregating the normalized hyperspectral profile of L8 and S2A.

The DaHD with TOA reflectance in the range of 0.04 – 0.2 across all spectral bands is used to develop the 4 angle hyperspectral BRDF model. The 4 angle hyperspectral BRDF model is further simplified to develop the DAHAC model by considering the significant coefficients in the model parameters. The simplified DAHAC model is leveraged to predict the TOA reflectance with a 10 nm spectral resolution and further subjected to cubic interpolation to achieve a finer 1 nm resolution. Thus, the DAHAC model can perform absolute calibration of any sensor with a 1 nm spectral resolution over the dark EPICS-Global.

The DAHAC model is validated with several multispectral sensors viz; L7 ETM+,

L8, and L9, S2A, and S2B. The validation results showed that the model is able to predict the TOA reflectance measurements with the highest accuracy of ±0.012 and precision within 0.02 unit reflectance for all spectral bands of Landsat missions (L7, L8, and L9). The model performance for Sentinel-2 missions (S2A and S2B) showed accuracy and precision within ±0.004 and ±0.02 unit reflectance. In contrast to the hyperspectral APICS model estimation accuracy within limited bands [1], the DAHAC model can predict the satellite measurements across all the spectral bands, especially for non-Landsat equivalent bands with higher accuracy. This result proves the DAHAC model is a robust tool for performing absolute calibration of any sensors on multispectral and hyperspectral instruments.

A thorough analysis is done to determine the model's overall uncertainty. Using the Monte Carlo simulation on the DAHAC model, the DAHAC model predicted TOA reflectance, and their standard deviation is estimated at different iteration levels. The DAHAC model uncertainty is found to be within 0.04 and 0.05 unit reflectance for VNIR and SWIR channels, respectively.

The sensors inter-comparison for the Landsat and Sentinel-2 missions is performed using the DAHAC model double ratio. The agreement between L8 and L9 is within 0.06% – 2%, and 1% for S2A and S2B. These results match closely with the results from L8-L9 cross-calibration (0.5% – 1%) [41], and S2A-S2B inter-comparison over Libya 4 (2%) [42].

The DAHAC model is capable of a nadir look angle of up to $10°$ and a solar zenith angle of up to $60°$, however; it would be more challenging for larger viewing angles. When the view zenith angle increases, the RSR shifts towards a shorter wavelength leading to bring changes in sensor received radiance information [43]. However, the RSR shift effect is not considered in this study. In addition, the DAHAC model does not consider factors

such as atmospheric scatterings, Rayleigh scattering, aerosol optical load, and gas absorption properties before developing the model.

However, increasing the DAHAC model's accuracy, decreasing its uncertainty, and improving the TOA reflectance consistency is still possible. The calibration variations between L8 and S2A with other sensors and random anomalies at the time of the sensor overpass due to atmospheric conditions are most likely the cause of the reduced accuracy. In general, the model accuracy can be improved by using more data samples with high-quality hyperspectral images for absolute calibration and sensor inter-comparison applications.

In the future, the proposed model development algorithm will be applied over stable bright sites to check its reliability and performance accuracy. The ability of the proposed algorithm to perform satellite absolute calibration will be tested for the dynamic range of TOA reflectance measurement. The RSR shift effect will also be considered during the absolute calibration model development with larger viewing angles of satellite data.

REFERENCES

[1] M. D. Chaity, M. Kaewmanee, L. Leigh, and C. Teixeira Pinto, "Hyperspectral empirical absolute calibration model using libya 4 pseudo invariant calibration site," *Remote Sensing*, vol. 13, no. 8, 2021, ISSN: 2072-4292. DOI: 10.3390/rs13081538. [Online]. Available: https://www.mdpi.com/2072-4292/13/8/1538.

[2] C. Bacour, X. Briottet, F.-M. Bréon, F. Viallefont-Robinet, and M. Bouvet, "Revisiting pseudo invariant calibration sites (pics) over sand deserts for vicarious calibration of optical imagers at 20 km and 100 km scales," *Remote Sensing*, vol. 11, no. 10, 2019, ISSN: 2072-4292. DOI: 10.3390/rs11101166. [Online]. Available: https://www.mdpi.com/2072-4292/11/10/1166.

[3] B. Raut, M. Kaewmanee, A. Angal, X. Xiong, and D. Helder, "Empirical absolute calibration model for multiple pseudo-invariant calibration sites," *Remote Sensing*, vol. 11, no. 9, 2019, ISSN: 2072-4292. DOI: 10.3390/rs11091105. [Online]. Available: https://www.mdpi.com/2072-4292/11/9/1105.

[4] N. Mishra, D. Helder, A. Angal, J. Choi, and X. Xiong, "Absolute calibration of optical satellite sensors using libya 4 pseudo invariant calibration site," *Remote Sensing*, vol. 6, no. 2, pp. 1327–1346, 2014, ISSN: 2072-4292. DOI: 10.3390/rs6021327. [Online]. Available: https://www.mdpi.com/2072-4292/6/2/1327.

[5] J. Fajardo Rueda, L. Leigh, C. Pinto, M. Kaewmanee, and D. Helder, "Classification and evaluation of extended pics (epics) on a global scale for calibration and stability monitoring of optical satellite sensors," *Remote Sensing*, vol. 13, p. 3350, Aug. 2021. DOI: 10.3390/rs13173350.

[6] M. Shrestha, L. Leigh, and D. Helder, "Classification of north africa for use as an extended pseudo invariant calibration sites (epics) for radiometric calibration and stability monitoring of optical satellite sensors," *Remote Sensing*, vol. 11, no. 7, 2019, ISSN: 2072-4292. DOI: 10.3390/rs11070875. [Online]. Available: https://www.mdpi.com/2072-4292/11/7/875.

[7] B. Markham, J. Barsi, G. Kvaran, *et al.*, "Landsat-8 operational land imager radiometric calibration and stability," *Remote Sensing*, vol. 6, no. 12, pp. 12 275–12 308, 2014, ISSN: 2072-4292. DOI: 10.3390/rs61212275. [Online]. Available: https://www.mdpi.com/2072-4292/6/12/12275.

[8] D. Helder, B. Basnet, and D. Morstad, "Optimized identification of worldwide radiometric pseudo-invariant calibration sites," *Canadian Journal of Remote Sensing*, vol. 36, pp. 527–539, Oct. 2010. DOI: 10.5589/m10-085.

[9] G. Chander, A. Angal, X. J. Xiong, *et al.*, "Preliminary assessment of several parameters to measure and compare usefulness of the CEOS reference pseudo-invariant calibration sites," in *Sensors, Systems, and Next-Generation Satellites XIV*, R. Meynart, S. P. Neeck, and H. Shimoda, Eds., International Society for Optics and Photonics, vol. 7826, SPIE, 2010, p. 78262L. DOI: 10.1117/12.865166. [Online]. Available: https://doi.org/10.1117/12.865166.

[10] H. Cosnefroy, M. Leroy, and X. Briottet, "Selection and characterization of saharan and arabian desert sites for the calibration of optical satellite sensors," *Remote Sensing of Environment*, vol. 58, no. 1, pp. 101–114, 1996, ISSN: 0034-4257. DOI: https://doi.org/10.1016/0034-4257(95)00211-1. [Online]. Available: https://www.sciencedirect.com/science/article/pii/0034425795002111.

[11] "Usgs eros archive - committee on earth observation satellites (ceos) legacy - calibration/validation test sites," eprint: https://www.usgs.gov/centers/eros/science/usgs-eros-archive-committee-earth-observation-satellites-ceos-legacy?qt-science_center_objects=0#qt-science_center_objects. [Online]. Available: https://www.usgs.gov/centers/eros/science/usgs-eros-archive-committee-earth-observation-satellites-ceos-legacy?qt-science_center_objects=0#qt-science_center_objects.

[12] D. Helder, K. J. Thome, N. Mishra, *et al.*, "Absolute radiometric calibration of landsat using a pseudo invariant calibration site," *IEEE Transactions on Geoscience and Remote Sensing*, vol. 51, no. 3, pp. 1360–1369, 2013. DOI: 10.1109/TGRS.2013.2243738.

[13] F. T. Z. Tuli, C. T. Pinto, A. Angal, X. Xiong, and D. Helder, "New approach for temporal stability evaluation of pseudo-invariant calibration sites (pics)," *Remote Sensing*, vol. 11, no. 12, 2019, ISSN: 2072-4292. DOI: 10.3390/rs11121502. [Online]. Available: https://www.mdpi.com/2072-4292/11/12/1502.

[14] H. Vuppula, "Normalization of pseudo-invariant calibration sites for increasing the temporal resolution and long-term trending," 2017.

[15] R. Shah, L. Leigh, M. Kaewmanee, and C. T. Pinto, "Validation of expanded trend-to-trend cross-calibration technique and its application to global scale," *Remote Sensing*, vol. 14, no. 24, 2022, ISSN: 2072-4292. DOI: 10.3390/rs14246216. [Online]. Available: https://www.mdpi.com/2072-4292/14/24/6216.

[16] Y. Govaerts and M. Clerici, "Evaluation of radiative transfer simulations over bright desert calibration sites," *Geoscience and Remote Sensing, IEEE Transactions on*, vol. 42, pp. 176 –187, Feb. 2004. DOI: 10.1109/TGRS.2003.815406.

[17] Y. Govaerts, S. Adriaensen, and S. Sterckx, "Optical sensor calibration using simulated radiances over desert sites," Jul. 2012. DOI: 10.1109/IGARSS.2012.6352568.

[18] R. Bhatt, D. R. Doelling, D. Morstad, B. R. Scarino, and A. Gopalan, "Desert-based absolute calibration of successive geostationary visible sensors using a daily exoatmospheric radiance model," *IEEE Transactions on Geoscience and Remote Sensing*, vol. 52, no. 6, pp. 3670–3682, 2014. DOI: 10.1109/TGRS.2013.2274594.

[19] R. Bhatt, D. R. Doelling, A. Wu, *et al.*, "Initial stability assessment of s-npp viirs reflective solar band calibration using invariant desert and deep convective cloud targets," *Remote Sensing*, vol. 6, no. 4, pp. 2809–2826, 2014, ISSN: 2072-4292. DOI: 10.3390/rs6042809. [Online]. Available: https://www.mdpi.com/2072-4292/6/4/2809.

[20] M. Kaewmanee and D. Helder, "Refined absolute pics calibration model over libya-4 using sentinel2a and landsat 8 collection-1 data for validation. in proceedings of the pecroa 20.,"

[21] "Landsat collection-1 level-1 product," eprint: https://docslib.org/doc/7625025/landsat-collection-1-level-1-product-definition. [Online]. Available: https://docslib.org/doc/7625025/landsat-collection-1-level-1-product-definition.

[22] M. M. Farhad, M. Kaewmanee, L. Leigh, and D. L. Helder, "Radiometric cross calibration and validation using 4 angle brdf model between landsat 8 and sentinel 2a," *Remote. Sens.*, vol. 12, p. 806, 2020.

[23] L. Leigh, M. Shrestha, N. Hasan, and M. Kaewmanee, "Classification of north africa for use as an extended pseudo invariant calibration site for radiometric calibration and stability monitoring of optical satellite sensors. in proceedings of the calcon 2019, utah state university, logan, ut, usa, 19–21 september 2019,"

[24] S. N. Goward, J. G. Masek, D. L. Williams, J. R. Irons, and R. Thompson, "The landsat 7 mission: Terrestrial research and applications for the 21st century," *Remote Sensing of Environment*, vol. 78, no. 1, pp. 3–12, 2001, Landsat 7, ISSN: 0034-4257. DOI: https://doi.org/10.1016/S0034-4257(01)00262-0. [Online]. Available: https://www.sciencedirect.com/science/article/pii/S0034425701002620.

[25] S. Andrefouet, R.Bindschadler, E. B. de Colstoun, *et al.*, "Preliminary assessment of the value of landsat-7 etm+ data following scan line corrector malfunction," *US Geological Survey, EROS Data Center*, 2003.

[26] "Usgs landsat-7 mission," eprint: https://www.usgs.gov/landsat-missions/landsat-7. [Online]. Available: https://www.usgs.gov/landsat-missions/landsat-7.

[27] "Landsat collection 2 level-1 data," eprint: https://www.usgs.gov/landsat-missions/landsat-collection-2-level-1-data. [Online]. Available: https://www.usgs.gov/landsat-missions/landsat-collection-2-level-1-data.

[28] "Landsat mission: Landsat-9," eprint: https://www.usgs.gov/landsat-missions/landsat-9. [Online]. Available: https://www.usgs.gov/landsat-missions/landsat-9.

[29] "Landsat 8 data users handbook. available online:," eprint: https://www.usgs.gov/landsat-missions/landsat-8-data-users-handbook. [Online]. Available: https://www.usgs.gov/landsat-missions/landsat-8-data-users-handbook.

[30] M. Drusch, U. Del Bello, S. Carlier, *et al.*, "Sentinel-2: Esa's optical high-resolution mission for gmes operational services," *Remote Sensing of Environment*, vol. 120, pp. 25–36, 2012, The Sentinel Missions - New Opportunities for Science, ISSN: 0034-4257. DOI: https://doi.org/10.1016/j.rse.2011.11.026. [Online]. Available: https://www.sciencedirect.com/science/article/pii/S0034425712000636.

[31] J. Li and D. P. Roy, "A global analysis of sentinel-2a, sentinel-2b and landsat-8 data revisit intervals and implications for terrestrial monitoring," *Remote Sensing*, vol. 9, no. 9, 2017, ISSN: 2072-4292. [Online]. Available: https://www.mdpi.com/2072-4292/9/9/902.

[32] C. Revel, V. Lonjou, S. Marcq, *et al.*, "Sentinel-2a and 2b absolute calibration monitoring," *European Journal of Remote Sensing*, vol. 52, pp. 122–137, Jan. 2019. DOI: 10.1080/22797254.2018.1562311.

[33] S. Ungar, J. Pearlman, J. Mendenhall, and D. Reuter, "Overview of the earth observing one (eo-1) mission," *IEEE Transactions on Geoscience and Remote Sensing*, vol. 41, no. 6, pp. 1149–1159, 2003. DOI: 10.1109/TGRS.2003.815999.

[34] X. Jing, L. Leigh, D. Helder, C. Teixeira Pinto, and D. Aaron, "Lifetime absolute calibration of the eo-1 hyperion sensor and its validation," *IEEE Transactions on Geoscience and Remote Sensing*, vol. 57, no. 11, pp. 9466–9475, 2019. DOI: 10.1109/TGRS.2019.2926663.

[35] S. Franks, C. S. R. Neigh, P. K. Campbell, *et al.*, "Eo-1 data quality and sensor stability with changing orbital precession at the end of a 16 year mission," *Remote Sensing*, vol. 9, no. 5, 2017, ISSN: 2072-4292. DOI: 10.3390/rs9050412. [Online]. Available: https://www.mdpi.com/2072-4292/9/5/412.

[36] E. Micijevic, M. O. Haque, and N. Mishra, "Radiometric calibration updates to the Landsat collection," in *Earth Observing Systems XXI*, J. J. Butler, X. J. Xiong, and X. Gu, Eds., International Society for Optics and Photonics, vol. 9972, SPIE, 2016, pp. 108 –119. DOI: 10.1117/12.2239426. [Online]. Available: https://doi.org/10.1117/12.2239426.

[37] "Landsat collection 2 quality assessment bands," eprint: https://www.usgs.gov/landsat-missions/landsat-collection-2-quality-assessment-bands. [Online]. Available: https://www.usgs.gov/landsat-missions/landsat-collection-2-quality-assessment-bands.

[38]   . eprint: https://www.mathworks.com/help/matlab/ref/interp1.html. [Online].
       Available: https://www.mathworks.com/help/matlab/ref/interp1.html.

[39]   J. A. Barsi, B. Alhammoud, J. Czapla-Myers, *et al.*, "Sentinel-2a msi and landsat-8
       oli radiometric cross comparison over desert sites," *European Journal of Remote
       Sensing*, vol. 51, no. 1, pp. 822–837, 2018. DOI: 10.1080/22797254.2018.1507613.
       eprint: https://doi.org/10.1080/22797254.2018.1507613. [Online]. Available:
       https://doi.org/10.1080/22797254.2018.1507613.

[40]   G. Gross, D. Helder, and L. Leigh, "Extended cross-calibration analysis using data
       from the landsat 8 and 9 underfly event," *Remote Sensing*, vol. 15, no. 7, 2023, ISSN:
       2072-4292. DOI: 10.3390/rs15071788. [Online]. Available:
       https://www.mdpi.com/2072-4292/15/7/1788.

[41]   G. Gross, D. Helder, C. Begeman, L. Leigh, M. Kaewmanee, and R. Shah, "Initial
       cross-calibration of landsat 8 and landsat 9 using the simultaneous underfly event,"
       Remote Sensing, vol. 14, no. 10, 2022, ISSN: 2072-4292. [Online]. Available:
       https://www.mdpi.com/2072-4292/14/10/2418.

[42]   S. Sterckx and E. Wolters, "Radiometric top-of-atmosphere reflectance consistency
       assessment for landsat 8/oli, sentinel-2/msi, proba-v, and deimos-1 over libya-4 and
       radcalnet calibration sites," *Remote Sensing*, vol. 11, no. 19, 2019, ISSN: 2072-4292.
       DOI: 10.3390/rs11192253. [Online]. Available:
       https://www.mdpi.com/2072-4292/11/19/2253.

[43]   Z. Cui and J. P. Kerekes, "Impact of wavelength shift in relative spectral response at
       high angles of incidence in landsat-8 operational land imager and future landsat
       design concepts," *IEEE Transactions on Geoscience and Remote Sensing*, vol. 56,
       no. 10, pp. 5873–5883, 2018. DOI: 10.1109/TGRS.2018.2827394.